

Power spectrum analysis for optical tweezers

Kirstine Berg-Sørensen^{a)}

The Niels Bohr Institute, Blegdamsvej 17, DK-2100 Copenhagen Ø, Denmark

Henrik Flyvbjerg^{b)}

Plant Research Department, Risø National Laboratory, DK-4000 Roskilde, Denmark

(Received 7 April 2003; accepted 1 December 2003)

The force exerted by an optical trap on a dielectric bead in a fluid is often found by fitting a Lorentzian to the power spectrum of Brownian motion of the bead in the trap. We present explicit functions of the experimental power spectrum that give the values of the parameters fitted, including error bars and correlations, for the best such χ^2 fit in a given frequency range. We use these functions to determine the information content of various parts of the power spectrum, and find, at odds with lore, much information at relatively high frequencies. Applying the method to real data, we obtain perfect fits and calibrate tweezers with less than 1% error when the trapping force is not too strong. Relatively strong traps have power spectra that cannot be fitted properly with *any* Lorentzian, we find. This underscores the need for better understanding of the power spectrum than the Lorentzian provides. This is achieved using old and new theory for Brownian motion in an incompressible fluid, and new results for a popular photodetection system. The trap and photodetection system are then calibrated simultaneously in a manner that makes optical tweezers a tool of precision for force spectroscopy, local viscometry, and probably other applications.

© 2004 American Institute of Physics. [DOI: 10.1063/1.1645654]

I. INTRODUCTION

Optical tweezers are used in many contexts in biological physics,¹ e.g., in single molecule studies of molecular motors^{2,3} and other proteins and polymers,^{4–7} and in surgery at the cellular level,⁸ to name a few. In some of these contexts, the tweezers are only used to grab and hold something. In other contexts, they are used to exert a prescribed force, or to measure force: pico-Newton forces are measured or exerted,^{4,7,9–11} local viscosity is measured,^{12–14} or properties of a system are deduced from the Brownian motion of its parts.^{15–17} While relative relationships for, e.g., force versus displacement can be calculated theoretically in a decent approximation,¹⁸ the absolute value of the force cannot. It depends too much on experimental circumstances. So calibration is necessary. Good calibration is also a test that the tweezers, detection system, and data acquisition work as they are supposed to. As tweezer technology evolves and applications multiply, the need for good calibration methods will undoubtedly grow.

There are a number of ways to calibrate optical traps. (We use *trap* and tweezers as synonyms.) They are discussed in several excellent texts.^{19–25} The most reliable procedure interprets the power spectrum of Brownian motion of a bead in the trap. This is conventionally done with the Einstein–Ornstein–Uhlenbeck theory of Brownian motion, which predicts a Lorentzian spectrum. The stochastic distribution of experimental spectral values about this Lorentzian is also known theoretically (Sec. III). This fact, and the simplicity of the Lorentzian form, permit us to give explicit analytical

results for the values of fitted parameters as functions of the experimental power spectrum (Sec. IV). Thus, when the power spectrum is legitimately modeled with a Lorentzian, these results fit it with ease, insight, and error bars on the parameter values found. The trap's strength is consequently known with precision that may be limited mainly by the calibration of the position detection system (Sec. V).

Very similar results might be obtained also when *aliasing* is taken into account (Sec. VI), but are not that interesting because the Lorentzian is a low-frequency approximation (Sec. VII) that can exploit only a fraction of the information content of the power spectrum (Sec. VIII). Even worse is the fact that even at intermediate trapping strengths some photodetection systems have no low-frequency window at all in which a Lorentzian can be fitted properly.

Thus a correct theory for the power spectrum is needed when the Lorentzian fails, and in general improves precision. We show that the power spectrum can be fully understood by combining known and new results on Brownian motion in incompressible fluids (Secs. IX–XII) with new results for typical photodetection systems (Sec. XIII). Once the effects of aliasing and antialiasing filters are accounted for (Sec. XIV), we have a procedure for how to calibrate tweezers (Secs. XV and XVI) which, e.g., adds decades of interpretable spectrum to local viscometry measurements. It makes details of the power spectrum of complex systems interpretable.¹⁷ And it may open up the way for new applications of tweezers by making them a tool of precision.

Thus the thrust of this article is theory for how to analyze experimental data, with examples of how this is done. Readers who might wish to apply this analysis to their own data may do so easily with our MATLAB program that fits and

^{a)}Electronic mail: berg@alf.nbi.dk

^{b)}Electronic mail: henrik.flyvbjerg@risoe.dk

plots at the click of a button. Reference 26 documents this program.

In Appendix A is a collection of notations and characteristic values of quantities in this article. Appendices B–D describe manipulations and tests of data which ensure that the data quality matches the precision that the theory can extract from good data. These procedures are an integral part of the practical application of our theoretical results. Appendix E explores how maximum likelihood estimation changes with the data compression we employ. Appendix F contains a long calculation. Appendices G and H expand on two technical points.

II. MATERIALS AND METHODS

The experimental data analyzed here were obtained with the optical tweezer setup described in Ref. 27. The laser light had wavelength $\lambda = 1064$ nm and positions were detected with a silicon *PIN* photodiode, S5981 from Hamamatsu, which is a popular choice because of its large active area, 10×10 mm. The trapped microsphere was from a batch of uniform microspheres from Bang Laboratories, Inc., catalog code No. PS04N, Bangs lot No. 1013, Inventory No. L920902A, with density of 1.050 g/ml and diameter of 1.05 ± 0.01 μm .²⁸

The equipment was tested for electronic and mechanical noise in two “null tests” described in Appendix B. These tests set a bound on electronic noise, on the laser beam’s pointing instability, and on much, but not all, mechanical noise. Crosstalk between *x*- and *y*-channel data was diagnosed and removed by a linear transformation described in Appendix C. A model-independent data analysis that tests our assumption of a harmonic trapping potential was done and is described in Appendix D. This test can indicate, but not prove, that the potential actually is harmonic, so its role is to warn us against analyzing data that seem to not satisfy this essential assumption. The data analyzed here pass this and another test [Fig. 1(b)] to perfection.

III. SIMPLE THEORY RECAPITULATED

The Einstein–Ornstein–Uhlenbeck theory of Brownian motion²⁹ describes the motion of the bead in a harmonic trapping potential with the following Langevin equation:

$$m\ddot{x}(t) + \gamma_0\dot{x}(t) + \kappa x(t) = (2k_B T \gamma_0)^{1/2} \eta(t), \quad (1)$$

given here in one dimension for simplicity. Here $x(t)$ is the trajectory of the Brownian particle, m is its mass, γ_0 its friction coefficient, $-\kappa x(t)$ the harmonic force from the trap, and $(2k_B T \gamma_0)^{1/2} \eta(t)$ a random Gaussian process that represents Brownian forces at absolute temperature T ; for all t and t' :

$$\langle \eta(t) \rangle = 0; \quad \langle \eta(t) \eta(t') \rangle = \delta(t - t'). \quad (2)$$

Stokes’s law for a spherical particle gives

$$\gamma_0 = 6\pi\rho\nu R, \quad (3)$$

where $\rho\nu$ is the fluid’s shear viscosity, ρ the fluid’s density, ν its kinematic viscosity, and R the sphere’s radius.

The characteristic time for loss of kinetic energy through friction, $t_{\text{inert}} \equiv m/\gamma_0$, is 1000 times shorter than our experimental time resolution at 16 kHz sampling rate. We consequently follow Einstein and drop the inertial term in Eq. (1), so it then reads

$$\dot{x}(t) + 2\pi f_c x(t) = (2D)^{1/2} \eta(t), \quad (4)$$

where the *corner frequency*,

$$f_c \equiv \kappa/(2\pi\gamma_0), \quad (5)$$

has been introduced, and Einstein’s equation,

$$D = k_B T / \gamma_0 \quad (6)$$

relating the diffusion constant, Boltzmann energy, and friction coefficient has been used.

After recording $x(t)$ for time T_{msr} , we Fourier transform $x(t)$ and $\eta(t)$,

$$\tilde{x}_k = \int_{-T_{\text{msr}}/2}^{T_{\text{msr}}/2} dt e^{i2\pi f_k t} x(t), \quad f_k \equiv k/T_{\text{msr}}, \quad k \text{ integer}. \quad (7)$$

Equation (4) gives the path as a function of noise,

$$\tilde{x}_k = \frac{(2D)^{1/2} \tilde{\eta}_k}{2\pi(f_c - if_k)}.$$

(When $\dot{x}(t)$ is Fourier transformed, partial integration gives a contribution from the ends of the interval of integration which we ignore. This leakage term (Ref. 30, Sec. 12.7) is truly negligible in our case because the power spectral density in Eq. (10) is a smooth function without spikes or other abrupt changes in value.)

From Eq. (2) it follows that

$$\langle \tilde{\eta}_k \rangle = 0; \quad \langle \tilde{\eta}_k^* \tilde{\eta}_\ell \rangle = T_{\text{msr}} \delta_{k,\ell}; \quad \langle |\tilde{\eta}_k|^4 \rangle = 2T_{\text{msr}}^2. \quad (8)$$

Since $\eta(t)$ is an uncorrelated Gaussian process, $(\text{Re } \tilde{\eta}_k)_{k=0,1,\dots}$ and $(\text{Im } \tilde{\eta}_k)_{k=1,2,\dots}$ are uncorrelated random variables with Gaussian distribution. Consequently, $(|\tilde{\eta}_k|^2)_{k=1,2,\dots}$ are uncorrelated non-negative random variables with *exponential* distribution. Hence so are experimental values for the power spectrum,

$$P_k^{(\text{ex})} \equiv |\tilde{x}_k|^2 / T_{\text{msr}} = \frac{D/(2\pi^2 T_{\text{msr}}) |\tilde{\eta}_k|^2}{f_c^2 + f_k^2} \quad (9)$$

for $k > 0$. Their expected value is a Lorentzian,

$$P_k \equiv \langle P_k^{(\text{ex})} \rangle = \frac{D/(2\pi^2)}{f_c^2 + f_k^2}, \quad (10)$$

and because $P_k^{(\text{ex})}$ is exponentially distributed,

$$\sigma[P_k^{(\text{ex})}] = \langle (P_k^{(\text{ex})} - P_k)^2 \rangle^{1/2} = P_k. \quad (11)$$

IV. LEAST-SQUARES FITTING OF LORENTZIAN

Experimentally, we sample $x(t)$ with frequency f_{sample} for time T_{msr} . From the resulting time series $x_j \equiv x(t_j)$, $j = 1, \dots, N$, we form the *discrete* Fourier transform,

$$\hat{x}_k \equiv \Delta t \sum_{j=1}^N e^{i2\pi f_k t_j} x_j = \Delta t \sum_{j=1}^N e^{i2\pi j k/N} x_j, \quad (12)$$

$k = -N/2 + 1, \dots, N/2$, where $\Delta t \equiv 1/f_{\text{sample}}$, $t_j = j\Delta t$, and $N\Delta t = T_{\text{msr}}$. This discrete Fourier transform is a good approximation to the continuous one, Eq. (7), for frequencies $|f_k| \ll f_{\text{sample}}$. Consequently, the experimental power spectrum

$$P_k^{(\text{ex})} \equiv |\hat{x}_k|^2 / T_{\text{msr}}$$

obeys the same statistics as $|\hat{x}_k|^2 / T_{\text{msr}}$; see Sec. VI for details.

Least-squares fitting in its simplest form presupposes that each data point is “drawn” from a Gaussian distribution and that different data points are statistically independent. The second condition is satisfied by P_k in Eq. (9), but the first is not, since P_k is exponentially distributed. The solution is *data compression*, which results in a smaller data set with less noise, and, by way of the central limit theorem, in normally distributed data.

Data compression by *windowing* is common and has its advantages.³⁰ When the number n_w of windows used is large, the values of the compressed power spectrum are statistically independent and Gaussian distributed, and can be used in the formulas below. Windowing always compresses to equidistant points on the frequency axis. “Blocking” is an alternative method without this constraint, and hence is useful for data display with the logarithmic frequency axis. It replaces a “block” of n_b consecutive data points $(f, P^{(\text{ex})}(f))$ with a single new “data point” $(\bar{f}, \bar{P}^{(\text{ex})}(\bar{f}))$, with coordinates that simply are block averages.³⁰ When n_b is so large that we can ignore terms of nonleading power in n_b , $\bar{P}^{(\text{ex})}(\bar{f})$ is Gaussian distributed with $\langle \bar{P}^{(\text{ex})}(\bar{f}) \rangle = P(\bar{f})$ and $\sigma(\bar{P}^{(\text{ex})}(\bar{f})) = P(\bar{f}) / \sqrt{n_b}$.

In the following, it is understood that data have been blocked (or windowed, or both), but we leave out the overbar to keep the notation simple. We fit by minimizing

$$\chi^2 = \sum_k \left(\frac{P_k^{(\text{ex})} - P_k}{P_k / \sqrt{n_b}} \right)^2 = n_b n_w \sum_k \left(\frac{P_k^{(\text{ex})}}{P_k} - 1 \right)^2;$$

see Appendix E for background. This χ^2 can be minimized analytically: The theoretical spectrum can be written $P_k = (a + b f_k^2)^{-1}$ with a and b positive parameters to be fitted, so χ^2 is a quadratic function of a and b . Minimization gives

$$f_c = (a/b)^{1/2} = \left(\frac{S_{0,1} S_{2,2} - S_{1,1} S_{1,2}}{S_{1,1} S_{0,2} - S_{0,1} S_{1,2}} \right)^{1/2}, \quad (13)$$

$$\begin{aligned} \frac{DT_{\text{msr}}}{2\pi^2} = 1/b &= \frac{S_{0,2} S_{2,2} - S_{1,2}^2}{S_{1,1} S_{0,2} - S_{0,1} S_{1,2}}, \\ \frac{\chi_{\text{min}}^2}{n_b} &= S_{0,0} - \frac{S_{0,1}^2 S_{2,2} + S_{1,1}^2 S_{0,2} - 2 S_{0,1} S_{1,1} S_{1,2}}{S_{0,2} S_{2,2} - S_{1,2}^2}, \end{aligned} \quad (14)$$

where we have introduced the sums

$$S_{p,q} \equiv \sum_k f_k^{2p} P_k^{(\text{ex})q}.$$

V. FROM MILLIVOLTS TO NANOMETERS: CALIBRATING LENGTH SCALES

Note that we fit both D and f_c to the power spectrum of the x coordinate, and, in an independent fit, to the power spectrum of the y coordinate. The position detection system's output has a somewhat arbitrary amplitude that depends linearly on laser power and the three independent amplifier settings for the voltages measured, $V_I - V_{II} - V_{III} + V_{IV}$, V_I

+ $V_{II} - V_{III} - V_{IV}$, and V_z defined in Appendix C. This results in three arbitrary measures of length, one for each direction, x , y , and z . We determine two of the three corresponding conversion factors to units of physical length by equating the fitted values for D , which is determined in arbitrary units, to the value in physical units known from Einstein's relation, Eq. (6).

The fitted values of D can be determined with high precision, as demonstrated below. Its value in physical units, however, is not known with similar precision in some biophysical experiments. While the temperature T can be known very well, the value of γ_0 is a source of error in Einstein's relation. Microspheres are commercially available with radius R known to within 1% and similar precision of the spherical shape, so Stokes law, Eq. (3), applies. But the value of the dynamic viscosity $\rho\nu$ of the fluid, in which the experiments take place, may not be known with the same precision. Additives such as glucose, BSA, and casein change the value of $\rho\nu$ dramatically. Five percent of glucose, e.g., changes the viscosity of water by a factor of 1.12.³² Similarly, 5% of NaCl changes the viscosity of water by a factor of 1.19. Such concentrations of additives occur, e.g., in studies of single kinesin molecules³³ and in studies of single myosin molecules.³⁴ In such cases it is better to determine the conversion factors from arbitrary units to physical units of length by independent measurements, as was done in, e.g., Refs. 23 and 35. The fitted values of D may then serve as either a check of consistency for the method, or as independent determination of the value of γ_0 , hence of $\rho\nu$, which may also be calculated if one knows the concentrations of additives and how they affect the viscosity.

VI. ALIASED LORENTZIAN

We will now understand the effect of finite sampling time better than we did in Sec. IV: In an experiment we sample $x(t)$ at discrete times $t_j = j\Delta t$, $\Delta t \equiv 1/f_{\text{sample}}$. We consequently solve Eq. (4) in the time interval $t_j \leq t \leq t_{j+1}$ for given noise to find the *effective* Einstein–Ornstein–Uhlenbeck theory for discretely sampled data. We find

$$x_{j+1} = c x_j + \Delta x \eta_j, \quad (15)$$

with

$$\langle \eta_j \rangle = 0; \quad \langle \eta_i \eta_j \rangle = \delta_{i,j} \quad \text{for all } i, j. \quad (16)$$

Here we have introduced

$$\eta_j \equiv \left(\frac{4\pi f_c}{1 - c^2} \right)^{1/2} \int_{t_j}^{t_{j+1}} dt e^{-2\pi f_c(t_{j+1} - t)} \eta(t), \quad (17)$$

$$c \equiv \exp(-\pi f_c / f_{\text{Nyq}}); \quad f_{\text{Nyq}} \equiv f_{\text{sample}}/2, \quad (18)$$

and

$$\Delta x \equiv \left(\frac{(1 - c^2)D}{2\pi f_c} \right)^{1/2}. \quad (19)$$

Application of the discrete Fourier transform, Eq. (12), to x and η in Eq. (15) transforms Eq. (15) to

$$e^{i2\pi k/N} \hat{x}_k = c \hat{x}_k + \Delta x \hat{\eta}_k, \quad (20)$$

while the Fourier transformed version of Eq. (16) is

$$\langle \hat{\eta}_k \rangle = 0; \quad \langle \hat{\eta}_k^* \hat{\eta}_\ell \rangle = T \Delta t \delta_{k,\ell} \quad (21)$$

for all $k, \ell \in \{N/2+1, \dots, N/2\}$. So now our experimental estimate for the power spectrum is

$$P_k^{(\text{ex})} = |\hat{x}_k|^2 / T = \frac{(\Delta x)^2 |\hat{\eta}_k|^2 / T}{1 + c^2 - 2c \cos(2\pi k/N)}. \quad (22)$$

The expected value for this spectrum is

$$P_k \equiv \langle P_k^{(\text{ex})} \rangle = \langle |\hat{x}_k|^2 / T \rangle = \frac{(\Delta x)^2 \Delta t}{1 + c^2 - 2c \cos(2\pi k/N)}, \quad (23)$$

and its root-mean-square deviation is

$$\sigma(P_k^{(\text{ex})}) = P_k, \quad (24)$$

identical in form to Eq. (11) because $|\hat{\eta}_k|^2$ like $|\tilde{\eta}_k|^2$ is exponentially distributed.

Equation (23) gives the function that replaces the Lorentzian in the case of finite sampling frequency, and it should fit the experimental spectrum for all frequencies of $0 < f_k \leq f_{\text{Nyq}}$ if the simple theory discussed here is correct. Least-squares fitting of Eq. (23) to experimental data can be done analytically, once and for all, and it results in expressions very similar to those in Sec. IV.

We note that for $f_c \ll f_{\text{Nyq}}$ and $|f_k| \ll f_{\text{Nyq}}$, Eq. (23) to leading order in f_c/f_{Nyq} and f_k/f_{Nyq} becomes the Lorentzian in Eq. (10). So the approximation done in Sec. IV when we fitted the Lorentzian to the experimental spectrum has now been understood within the same simple theory for Brownian motion by accounting for the finite sampling frequency. The effect of the latter is maximal at $f_{\text{Nyq}} = f_{N/2}$ where, for same f_c and D , $P_{N/2} = 2.47 P(f_{N/2})$, i.e., at f_{Nyq} the finite sampling rate increases the power spectrum by 247% over its Lorentzian value.

With this understanding, it seems more correct to replace the Lorentzian altogether with Eq. (23), the so-called *aliased Lorentzian*; see Appendix H for more about aliasing. More so because so-called antialiasing filters do *not* change the aliased Lorentzian back into a Lorentzian; see Fig. 11. The outcome of this replacement can be determined without actually doing it from a simple phenomenological plot of the experimental power spectrum. If an aliased Lorentzian fits the experimental power spectrum $P_k^{(\text{ex})}$, a plot of $P_k^{(\text{ex})-1}$ vs $\cos(2\pi k/N)$ falls onto a straight line, according to Eq. (23). Figure 1 shows our experimental power spectrum plotted in this manner. Clearly, the data points do not fall onto a straight line. They do increasingly for smaller beads and sampling rates, especially for a different photodetection system and/or shorter laser wavelength, as explained below.

VII. LIMITS ON LORENTZIANS

Over which range of frequencies f_k should the sums $S_{p,q}$ be done? Stochastic errors are minimized by maximizing this range, but systematic errors limit the range: At low frequencies the experimental power spectrum typically is contaminated by low-frequency noise external to the experiment; see Appendix B. At high frequencies there are three concerns: (i) The Lorentzian is a good approximation only for $f^2 \ll f_{\text{Nyq}}^2$, where $f_{\text{Nyq}} \equiv f_{\text{sample}}/2$, as we have seen. As we have also

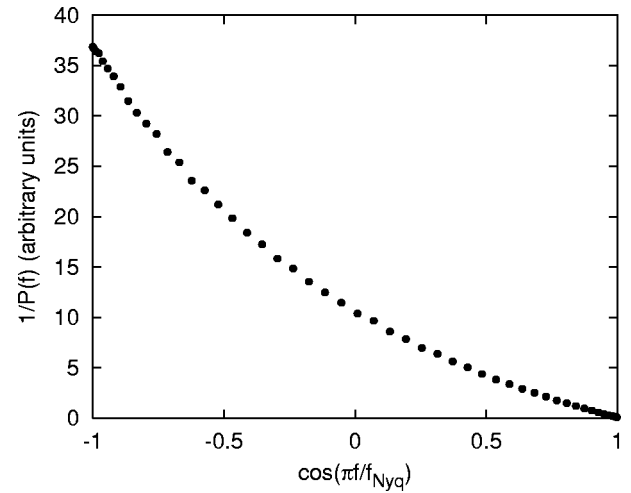


FIG. 1. Inverse experimental power spectrum, $P_k^{(\text{ex})-1}$ plotted vs $\cos(\pi f/f_{\text{Nyq}})$. Plotted this way, an aliased Lorentzian form would fall onto a straight line, see Eq. (23). In case one uses an oversampling delta-sigma data converter, aliasing and electronic filtering do not occur below the output frequency. So for that case one should plot $P_k^{(\text{ex})-1}$ vs f^2 . Then a pure Lorentzian form falls onto a straight line, and effects of frequency-dependent hydrodynamical friction and unintended filtering (see Secs. IX–XIII) show up as curvature.

seen, one can trade this approximation for an exact result, an aliased Lorentzian, but the latter does not describe the data. Other effects are in play. (ii) Some position detection systems, including ours, unintentionally cause significant low-pass filtering.³⁶ (iii) The Einstein–Ornstein–Uhlenbeck theory of Brownian motion is only a low-frequency approximation when used for liquids; the hydrodynamically correct spectrum is not Lorentzian.

Thus one should fit with a Lorentzian in an interval $[f_{\min}, f_{\max}]$ that avoids these systematic errors at high and low frequencies while minimizing stochastic errors of the fitted parameters. To this end, we give the stochastic errors' dependence on $[f_{\min}, f_{\max}]$.

VIII. INFORMATION CONTENT OF THE SPECTRUM

Given Eqs. (13) and (14), propagation of errors gives (see Appendix F)

$$\frac{\sigma(f_c)}{f_c} = \frac{s_{f_c}(x_{\min}, x_{\max})}{\sqrt{\pi f_c T_{\text{msr}}}}, \quad (25)$$

$$\frac{\sigma(D)}{D} = \left(\frac{1 + \pi/2}{\pi f_c T_{\text{msr}}} \right)^{1/2} s_D(x_{\min}, x_{\max}), \quad (26)$$

and the covariance $\langle (f_c - \langle f_c \rangle)(D - \langle D \rangle) \rangle \equiv \langle f_c D \rangle_c$ is

$$\frac{\langle f_c D \rangle_c}{\sigma(f_c) \sigma(D)} = \left(\frac{v(x_{\min}, x_{\max})}{u(x_{\min}, x_{\max})} \right)^{1/2}.$$

Here, $x_{\min} \equiv f_{\min}/f_c$, $x_{\max} \equiv f_{\max}/f_c$, and we have introduced the dimensionless functions,

$$s_{f_c}(x_1, x_2) \equiv \left(\frac{\pi}{u(x_1, x_2) - v(x_1, x_2)} \right)^{1/2}, \quad (27)$$

$$s_D(x_1, x_2) \equiv \left(\frac{u(x_1, x_2)}{(1 + \pi/2)(x_2 - x_1)} \right)^{1/2} s_{f_c}(x_1, x_2),$$

$$u(x_1, x_2) \equiv \frac{2x_2}{1+x_2^2} - \frac{2x_1}{1+x_1^2} + 2 \arctan\left(\frac{x_2 - x_1}{1+x_1x_2}\right),$$

$$v(x_1, x_2) \equiv \frac{4}{x_2 - x_1} \arctan^2\left(\frac{x_2 - x_1}{1+x_1x_2}\right). \quad (28)$$

The function s_{f_c} is normalized such that $s_{f_c}(0, \infty) = 1$. Thus $s_{f_c}(x_{\min}, x_{\max}) \geq 1$, because maximum precision is achieved only by fitting to the whole spectrum. Less will do in practice, and do well, as Figs. 2 and 3 illustrate.

Figure 2 has $f_c = 357$ Hz, $f_{\min} = 110$ Hz, and $f_{\max} = 1$ kHz, hence $s_{f_c}(x_{\min}, x_{\max}) = s_{f_c}(0.31, 2.80) = 2.4$. For comparison, $s_{f_c}(0, 2.80) = 1.8$. So, given our value for f_{\max} , our nonvanishing value for f_{\min} costs us a 30% increase in the error bar for the value we find for f_c . On the other hand, $s_{f_c}(0.31, \infty) = 1.26$. So, given our value for f_{\min} , by increasing f_{\max} we could reduce the stochastic error for f_c by almost a factor of 2, if systematic errors did not prevent this. This is despite $f_{\max} \approx 3f_c$. To harvest this extra information, one needs a better understanding of the power spectrum at these frequencies than the Lorentzian provides.

Systematic errors may leave no frequency range at all in which one can properly fit a Lorentzian. A data set with almost twice larger corner frequency illustrates this, although it is sampled three times faster. When a Lorentzian is fitted to this power spectrum, f_c decreases as f_{\max} is increased, and support for the fit vanishes although $f_{\max}^2 \ll f_{\text{Nyq}}^2$ is satisfied; see Table I. In this case, proper calibration is impossible without better understanding of the power spectrum than the Lorentzian provides. Below, this understanding is provided, and calibration is achieved using the very same data set.

IX. FRICTION FELT BY A MICROSPHERE MOVING IN AN INCOMPRESSIBLE FLUID

When a rigid body moves through a dense fluid like water, the friction between the body and fluid depends on the body's past motion, since that determines the fluid's present motion. For a sphere performing linear harmonic motion $x(t)$ with cyclic frequency $\omega = 2\pi f$ in an incompressible fluid and at vanishing Reynold's number, the (Navier-) Stokes equations were solved analytically and give a "frictional" force,^{37,38}

$$F_{\text{fric}} = -\gamma_0 \left(1 + \frac{R}{\delta} \right) \dot{x} - \left(3\pi\rho R^2 \delta + \frac{2}{3}\pi\rho R^3 \right) \ddot{x}, \quad (29)$$

where only the term containing \ddot{x} dissipates energy; the term containing \dot{x} is inertial force from entrained fluid. The notation is the same as above: γ_0 is the friction coefficient of Stokes' law for linear motion with constant velocity, Eq. (3), $\rho = 1.0$ g/cm is the density of water at room temperature, $\nu = 1.0 \mu\text{m}^2/\text{s}$ is the kinematic friction coefficient of water, and $2R = 1.05 \mu\text{m}$ is the diameter of the sphere we used. Thus $\gamma_0 = 9 \times 10^{-6}$ g/s. The penetration depth δ character-

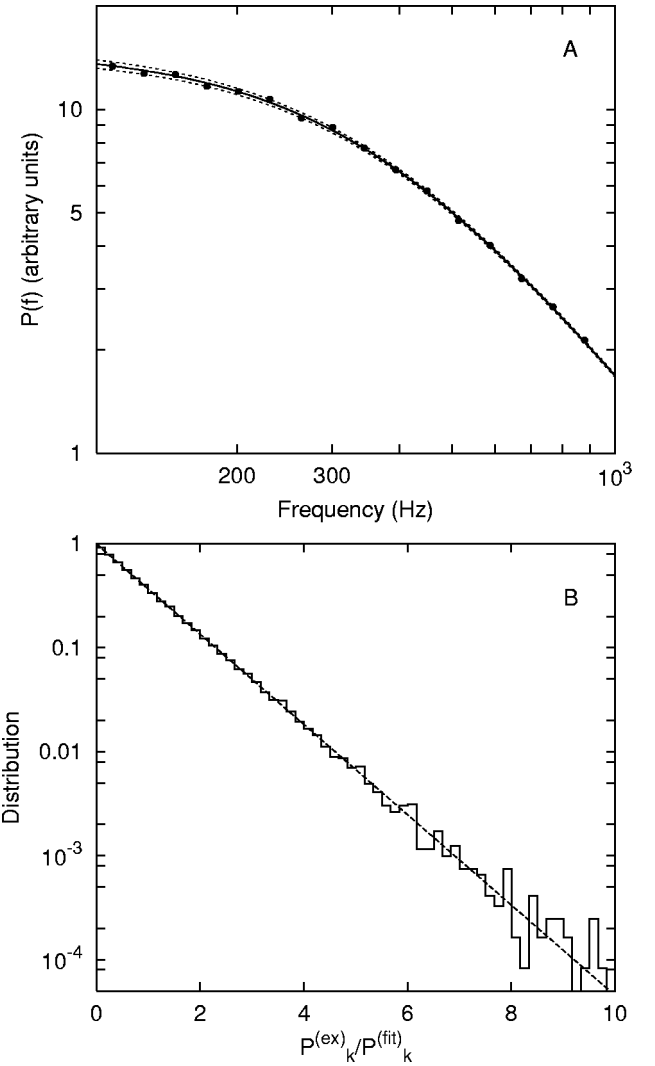


FIG. 2. (a) Lorentzian fitted to a power spectrum in the interval [110 Hz, 1 kHz] yielding $f_c = 357 \pm 3$ Hz and $D = 585 \pm 4$ (arb units)²/s. (The position detection system's arbitrary units of length are calibrated in Sec. V.) The power spectrum in this interval, already an average of $n_w = 5$ spectra, was blocked by a factor of $n_b = 517$ to $N' = 29$ points evenly distributed on the linear axis, then fitted using Eqs. (13) and (25). Dashed lines indicate \pm one standard deviation of the theoretical curve. Statistical support (Refs. 30 and 31) for the fit shown here is 60%. The experimental spectrum has $f_{\text{Nyq}} = 8$ kHz. (b) Histogram of $P_k^{(\text{ex})}/P_k^{(\text{fit})}$ for f_k in the frequency range of the fit, $P_k^{(\text{ex})}$ the unblocked experimental power-spectral values at f_k , and P_k its expected value, the fitted theory's value at f_k . According to theory, Eqs. (6) and (7), this ratio is exponentially distributed. Dashed line: $y = \exp(-x)$. Perfect agreement between theory and data is seen over all four decades of probability shown.

izes the exponential decrease of the fluid's velocity field as a function of the distance from the oscillating sphere. It is frequency dependent,

$$\delta(f) = (\nu/\pi f)^{1/2} = R(f_\nu/f)^{1/2}, \quad (30)$$

and large compared to R for the frequencies we consider, $f_\nu \equiv \nu/(\pi R^2) = 1.3$ MHz. This and other notations are given in Appendix A.

X. BEYOND EINSTEIN: BROWNIAN MOTION IN AN INCOMPRESSIBLE FLUID

Since Fourier decomposition describes any trajectory as a sum of linear oscillatory motions, the friction in Eq. (29)

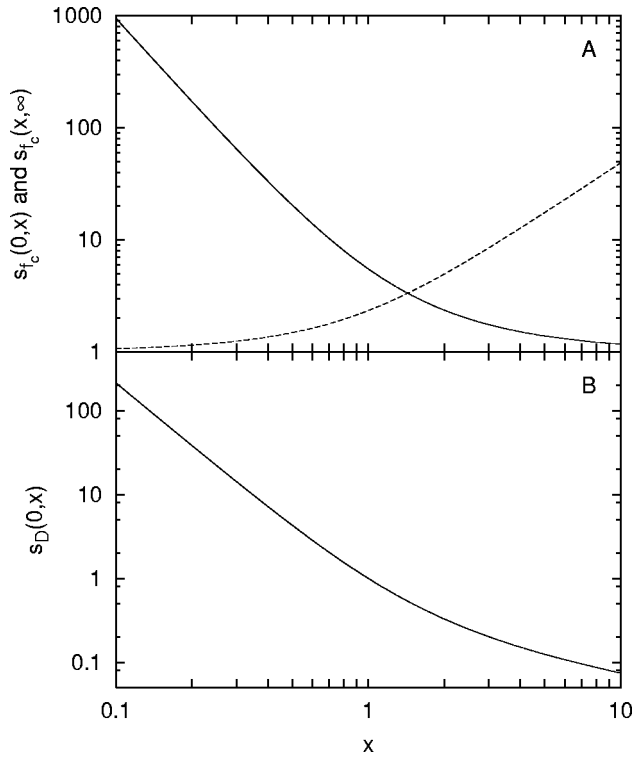


FIG. 3. (a) Ratio $s_{fc}(x_{\min}, x_{\max})$ between $\sigma(f_c)$ and the theoretical minimum for $\sigma(f_c)$, the former from a fit of a Lorentzian to an experimental power spectrum in the interval $[f_{\min}, f_{\max}]$, the latter from fitting to the same spectrum in $[0, \infty]$, assuming it is known there. Solid line: $s_{fc}(0, x_{\max})$ vs $x = x_{\max} = f_{\max}/f_c$. Dashed line: $s_{fc}(x_{\min}, \infty)$ vs $x = x_{\min} = f_{\min}/f_c$. Here $x_{\max} = \infty$ only means that f_{\max} is so much larger than f_c that the experimental spectrum's information content regarding f_c is essentially exhausted. Thus one can simultaneously have $f_{\max}^2 \ll f_{\text{Nyq}}^2$, ensuring aliasing is negligible for $f \leq f_{\max}$. Note that $s_{fc}(1, \infty) < s_{fc}(0, 2)$, i.e., there is more information about the f_c value in interval (f_c, ∞) than in interval $(0, 2f_c)$. (b) Graph of $s_D(0, x)$ showing $\sigma(D)/D$ vanishes as $x_{\max} \rightarrow \infty$, where $s_D(0, x) \sim x_{\max}^{-(1/2)}$ according to Eq. (28). Both (a) and (b) illustrate the great amount of information located in the high-frequency part of the spectrum.

also appears in the frequency representation of the *generalized Langevin equation* describing the Brownian motion of a harmonically trapped sphere in an incompressible fluid,³⁹

$$\begin{aligned} & [m(-i2\pi f)^2 + \gamma_{\text{Stokes}}(f)(-i2\pi f) + \kappa]\tilde{x}(f) \\ & = [2k_B T \text{Re } \gamma_{\text{Stokes}}(f)]^{1/2} \tilde{\eta}(f), \end{aligned} \quad (31)$$

$$\gamma_{\text{Stokes}}(f) = \frac{F_{\text{fric}}}{i2\pi f \tilde{x}(f)} = \gamma_0 \left(1 + (1-i) \frac{R}{\delta} - i \frac{2R^2}{9\delta^2} \right),$$

which becomes Einstein–Ornstein–Uhlenbeck theory, Eq. (1), in the limit of $f \rightarrow 0$. Here, as above, m is the mass of the

TABLE I. Parameter values of the Lorentzian fit (not shown) as a function of f_{\max} . The experimental power spectrum fitted to was obtained at a larger laser intensity than the spectrum shown in Fig. 2 and $f_{\text{sample}} = 25$ kHz. Data points in the experimental power spectrum were blocked to 750 equidistant points in the range of 110 Hz–25 kHz before fitting the Lorentzian to the points in the interval $[f_{\min}, f_{\max}]$ with $f_{\min} = 110$ Hz and f_{\max} listed.

f_{\max} (kHz)	f_c (Hz)	D (arb units) ² /s	Support (%)
1	641 ± 10	429 ± 9	37
2	630 ± 6	420 ± 4	9
3	610 ± 5	405 ± 2	0

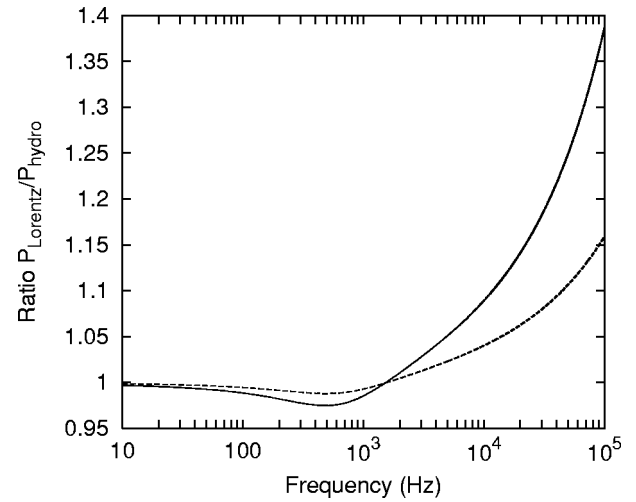


FIG. 4. Ratio between the Lorentzian power spectrum and the hydrodynamically correct power spectrum $P_{\text{hydro}}(f)$ in Eq. (32) evaluated with same parameter value $f_c = 666$ Hz. Solid line: Case of $2R = 1.05 \mu\text{m}$ like that in this article. Dashed line: Case of $2R = 500$ nm. Simple Einstein–Ornstein–Uhlenbeck theory is a better approximation for smaller objects and at lower frequencies. A change in f_c to ≈ 370 Hz does not change these curves at higher frequencies, but shifts the location of their minima to values just below the new value for f_c .

sphere, κ the spring constant of the harmonic trapping force, $k_B T$ the Boltzmann energy, Re denotes the “real part of,” and $\tilde{\eta}(f)$ is the Fourier transform of an uncorrelated random process $\eta(t)$, normalized like in Eq. (2) in order to show explicitly the frequency dependence of the Brownian noise that makes up the right-hand side of Eq. (31).

Experimentally, we monitor $x(t)$ for a long, but finite, time T_{msr} . Fourier transformation on this time interval, Eq. (7), gives the experimental power spectrum,

$$P_k^{(\text{ex})} = \frac{|\tilde{x}_k|^2}{T_{\text{msr}}} = \frac{2k_B T \text{Re } \gamma_{\text{Stokes}}(f_k) |\tilde{\eta}_k|^2 / T_{\text{msr}}}{|\kappa - i2\pi f_k \gamma_{\text{Stokes}}(f_k) - m(2\pi f_k)^2|^2},$$

where $(|\tilde{\eta}_k|^2)_{k=1,2,\dots}$, are uncorrelated non-negative random variables with exponential distribution that satisfy Eq. (8). Thus $(P_k^{(\text{ex})})_{k=1,2,\dots}$, are uncorrelated non-negative exponentially distributed random variables, each of which consequently has RMSD equal to its expected value. This property is unchanged by the filtering and aliasing applied below.

The expected value of $P_k^{(\text{ex})}$ is

$$P_{\text{hydro}}(f) = \frac{D/(2\pi^2)[1 + (f/f_v)^{1/2}]}{(f_c - f^{3/2}/f_v^{1/2} - f^2/f_m)^2 + (f + f^{3/2}/f_v^{1/2})^2}, \quad (32)$$

where $f_m \equiv \gamma_0/(2\pi m^*) \approx 3f_v/2 = 1.9$ MHz since $m^* \equiv m + 2\pi\rho R^3/3 \approx 3m/2$ for the polystyrene bead we use. (This simple relation between f_m and f_v might tempt one to eliminate one of these frequencies in favor of the other. They parameterize different physics however, f_v parameterizes the flow pattern established around a sphere undergoing linear harmonic oscillations in an incompressible fluid. This pattern is unrelated to the mass of the sphere. It need not have any, for that matter. f_m parameterizes the time it takes for friction to dissipate the kinetic energy of the sphere and the fluid it entrains. It depends on the mass of the sphere. By keeping both parameters in formulas, the physical origin of various terms remains clear.) This power spectrum contains the same two fitting parameters, f_c and D , as the Lorentzian of

the Einstein–Ornstein–Uhlenbeck theory, but differs significantly from it, except at low frequencies, as shown in Fig. 4. The radius R of the bead now also occurs in f_v and f_m , and not only through f_c , but it is not a parameter we must fit, because it is known to 1% uncertainty, and occurs only in terms that are so small that this small uncertainty of R has negligible effect on $P_{\text{hydro}}(f)$.

XI. FAXÉN'S FORMULA GENERALIZED TO LINEAR HARMONIC MOTION

The frictional force in Eq. (29) was derived by Stokes under the assumption that the oscillating sphere is infinitely

deep inside the fluid volume. For optimal designs, the lens that focuses the light into an optical trap typically has a short focal length. So a microsphere caught in such a trap is typically near a microscope coverslip. Consequently, the hydrodynamical interaction between the microsphere and the essentially infinite surface of the coverslip must be accounted for. Faxén has done this for a sphere moving parallel to an infinite plane with *constant* velocity in an incompressible fluid bounded by the plane and asymptotically at rest at conditions of vanishing Reynold's number. Solving perturbatively in R/ℓ , where ℓ is the distance from the sphere's center to the plane, Faxén found,^{40,41}

$$\gamma_{\text{Faxén}}(R/\ell) = \frac{\gamma_0}{1 - (9R/16\ell) + (R^3/8\ell^3) - (45R^4/256\ell^4) - (R^5/16\ell^5) + \dots}.$$

There is no second-order term in the denominator, so this formula remains good to within 1% for $\ell > 3R$ if one ignores all but the first-order term. This first-order result was first obtained by Lorentz.⁴² If his first-order calculation is repeated for a sphere undergoing linear oscillating motion parallel to a plane, one finds a friction formula that has Stokes' and Lorentz's as limiting cases⁴³

$$\gamma(f, R/\ell) = \gamma_{\text{Stokes}}(f) \left(1 + \frac{9}{16} \frac{R}{\ell} \times \left[1 - \frac{1-i}{3} \frac{R}{\delta} + \frac{2i}{9} \left(\frac{R}{\delta} \right)^2 - \frac{4}{3} (1 - e^{-(1-i)(2\ell-R)/\delta}) \right] \right). \quad (33)$$

The effect of the infinite plane is to increase friction, but less so at larger frequencies where δ is smaller.

We measured ℓ by first focusing the microscope on the coverslip surface. Having established $\ell=0$, the distance ℓ to the bead was determined with software provided for the microscope (Leica DM IRBE) by Leica. The software computes the distance moved by the oil-immersion microscope objective. This distance multiplied with the ratio of the refractive index of water to that of glass, 1.33/1.5, gives distance ℓ . The software gives ℓ within precision of 0.1 μm , to which must be added the independent error for determination of $\ell=0$, which is also 0.1 μm , we found, from repeated determinations.

We had $R/\ell \approx 1/12$ when it was largest. So the bead's hydrodynamic interaction with the coverslip has an effect of 4% or less, large enough that we must account for it. Fortunately, this introduces no new fitting parameters, because we know the value of ℓ . Since ℓ occurs only in a term of at most 4% relative importance, any error in ℓ value affects the final result with a 0.04 times smaller error, in our case by one per mil, at most.

XII. PHYSICAL POWER SPECTRUM

By replacing $\gamma_{\text{Stokes}}(f)$ with $\gamma(f, R/\ell)$ in Eqs. (29) and (31), one obtains a power spectrum that accounts for all relevant physics of the bead in the trap, with the expected value

$$P_{\text{hydro}}(f; R/\ell) = \frac{D/(2\pi^2) \text{Re } \gamma/\gamma_0}{(f_c + f \text{Im } \gamma/\gamma_0 - f^2/f_m)^2 + (f \text{Re } \gamma/\gamma_0)^2}, \quad (34)$$

where

$$\begin{aligned} \text{Re } \gamma/\gamma_0 &= 1 + \sqrt{f/f_v} - \frac{3R}{16\ell} \\ &+ \frac{3R}{4\ell} \exp\left(-\frac{2\ell}{R} \sqrt{f/f_v}\right) \cos\left(\frac{2\ell}{R} \sqrt{f/f_v}\right) \end{aligned}$$

and

$$\begin{aligned} \text{Im } \gamma/\gamma_0 &= -\sqrt{f/f_v} + \frac{3R}{4\ell} \\ &\times \exp\left(-\frac{2\ell}{R} \sqrt{f/f_v}\right) \sin\left(\frac{2\ell}{R} \sqrt{f/f_v}\right). \end{aligned}$$

We refer to this as the *physical* power spectrum. It differs from the *recorded* power spectrum because the data acquisition system contains filters, some intended, some not, and because the data acquisition system samples the resulting *filtered* spectrum only at discrete times to produce the spectrum recorded. Below, we discuss the effects of filtering and finite sampling frequency.

XIII. POSITION DETECTION SYSTEM IS A LOW-PASS FILTER

Silicon is transparent to infrared light. For this reason, position detection systems like ours have finite response times of the order of tens of microseconds. The delayed part of the signal decreases over time as a simple exponential, so our diode's characteristics is a sum of two terms:³⁶ (i) a

small constant $\alpha^{(\text{diode})2}$, corresponding to the fraction $\alpha^{(\text{diode})}$ of response that is instantaneous, and (ii) a Lorentzian, corresponding to the delayed response,

$$\frac{P(f)}{P_0(f)} = \alpha^{(\text{diode})2} + \frac{1 - \alpha^{(\text{diode})2}}{1 + (f/f_{3\text{ dB}}^{(\text{diode})})^2}. \quad (35)$$

The parameters $\alpha^{(\text{diode})}$ and $f_{3\text{ dB}}^{(\text{diode})}$ depend on (i) the laser's wavelength and intensity, (ii) the photodiode's thickness, material properties, and reverse bias, and (iii) line up of the laser beam and photodiode.^{36,44,45} Consequently, the optimal way in which to determine the values of $f_{3\text{ dB}}^{(\text{diode})}$ and $\alpha^{(\text{diode})}$ relevant for a recorded spectrum is to include them with f_c and D as third and fourth fitting parameters in a fit to the spectrum. The logic of this procedure is sound, even though we calibrate the position detection system with the same data from which we want to calibrate the trap; see Appendix G for details.

For the position detection system analyzed here, Eq. (35) describes the filtering effect of this system out to approximately 30 kHz with the precision achieved here. We used zero reverse bias across the photodiode. With reverse bias, Eq. (35) is good out to larger frequencies. In general, the filtering effect of the position detection system at larger frequencies is described by a more complicated expression than Eq. (35), an expression that accounts also for faster decreasing solutions to the diffusion equation for charge carriers in the photodiode.⁴⁴

XIV. ALIASING AND ANTIALIASING FILTERS

Sampling of the power spectrum with finite sampling rate causes *aliasing*. Data acquisition electronics typically have built-in antialiasing filters. Delta-sigma data conversion systems use oversampling and “noise-shaping” filters to eliminate aliasing altogether, and the effect of their built-in filters is only seen near their readout frequency. Section XIV can be skipped by those using such data acquisition systems. For others, aliasing, antialiasing filters, and how they relate are discussed in some detail in Appendix H. An important point made there is that antialiasing filters do not prevent all aliasing, they do not prevent the aliasing accounted for here with Eq. (37).

Our data acquisition electronics have two built-in antialiasing filters, both first-order filters with roll-off frequencies, $f_{3\text{ dB}}$, that we set as high as possible, 80 and 50 kHz, respectively. This is not the normal recommended setting, but it gives optimal conditions for observation of the physics of the problem and of unintentional filtering by the position detection system.

A first-order filter reduces the power of its input, $P_0(f)$, by a factor of

$$\frac{P(f)}{P_0(f)} = \frac{1}{1 + (f/f_{3\text{ dB}})^2}. \quad (36)$$

The effect of filters, intended or not, is accounted for by multiplying the physically correct power-spectral expected value in Eq. (34) with the characteristic function for each filter, i.e., with Eqs. (35) and (36)—the latter twice, once for

each of our filters. That done, aliasing is accounted for by summing the result, $P^{(\text{filtered})}$, over aliased frequencies,

$$P^{(\text{aliased})}(f) = \sum_{n=-\infty}^{\infty} P^{(\text{filtered})}(f + nf_{\text{sample}}), \quad (37)$$

where in practice a finite number of terms exhausts the sum. The result, $P^{(\text{aliased})}(f)$, is our theory for the expected value of the experimental power spectrum recorded.

XV. HOW TO CALIBRATE TWEEZERS

The procedure described here in Sec. XV is implemented in freely available MATLAB software documented in Ref. 26.

The experimental spectrum to which we fitted in Fig. 5 is the result of *blocking*³⁰ a spectrum that is the average of five spectra, which were calculated from five time series recorded in five time windows, each with duration of $2^{18}\Delta t \approx 16\text{ s}$ ($\Delta t = 1/f_{\text{sample}} = 1/16\,000\text{ s}$). Similarly, Fig. 6 is based on four such time windows, each with duration of $2^{18}\Delta t \approx 5\text{ s}$ ($\Delta t = 1/f_{\text{sample}} = 1/50\,000\text{ s}$). In both cases consecutive windows were separated by several minutes. A study of power spectra and fitted parameters obtained from individual windows showed that neither drifted between windows, although the center of the trap did. Thus it is legitimate to average over five/four spectra as we did. The spectrum thus obtained was blocked on the linear frequency axis to $N' = 150$ data points, with each block containing approximately 870 points. Before any blocking was done, crosstalk between channels was eliminated in the manner described in Appendix C.

Our theory for the expected value of the power spectrum was fitted to the recorded experimental power spectrum using our theory for the scatter of the latter about the former: It scatters with standard deviation proportional to its expected value, i.e., Eqs. (E4) and (E5) apply with n_b replaced by $n_b n_w$, $n_w = 5$ (4), as described in Appendix E. Thus we fit by minimizing

$$\chi^2 = \sum_{k=1}^{N'} \left(\frac{P_k^{(\text{ex})} - P_k}{P_k / \sqrt{n_w n_b}} \right)^2 = n_w n_b \sum_{k=1}^{N'} \left(\frac{P_k^{(\text{ex})}}{P_k} - 1 \right)^2, \quad (38)$$

where the sum is over blocked data points and $N' \equiv N/(n_w n_b)$. The form of χ^2 does not suit standard least-squares fitting routines. However, exact rewriting yields a form that does,

$$\chi^2 = \sum_{k=1}^{N'} \left(\frac{P_k^{-1} - P_k^{(\text{ex})-1}}{\sigma_k} \right)^2 \quad (39)$$

where $\sigma_k = P_k^{(\text{ex})-1}/(n_w n_b)^{1/2}$.

The solid line in Fig. 5(a) [Fig. 6(a)] shows $P_{\text{hydro}}(f; R/l)$, multiplied by the characteristic functions of the diode and electronic filters, aliased with $f_{\text{sample}} = 16\text{ kHz}$ [50 kHz], then fitted to the experimental spectrum using f_c , D , $f_{3\text{ dB}}^{(\text{diode})}$, and $\alpha^{(\text{diode})}$ as fitting parameters. The parameter values obtained from these least-squares fits are listed in Tables II and III. We see that both the strength of the trap, in the form of f_c , and conversion of the position detection system's arbitrary units to nanometers, are determined to within 1% precision or better. The latter conversion was found by

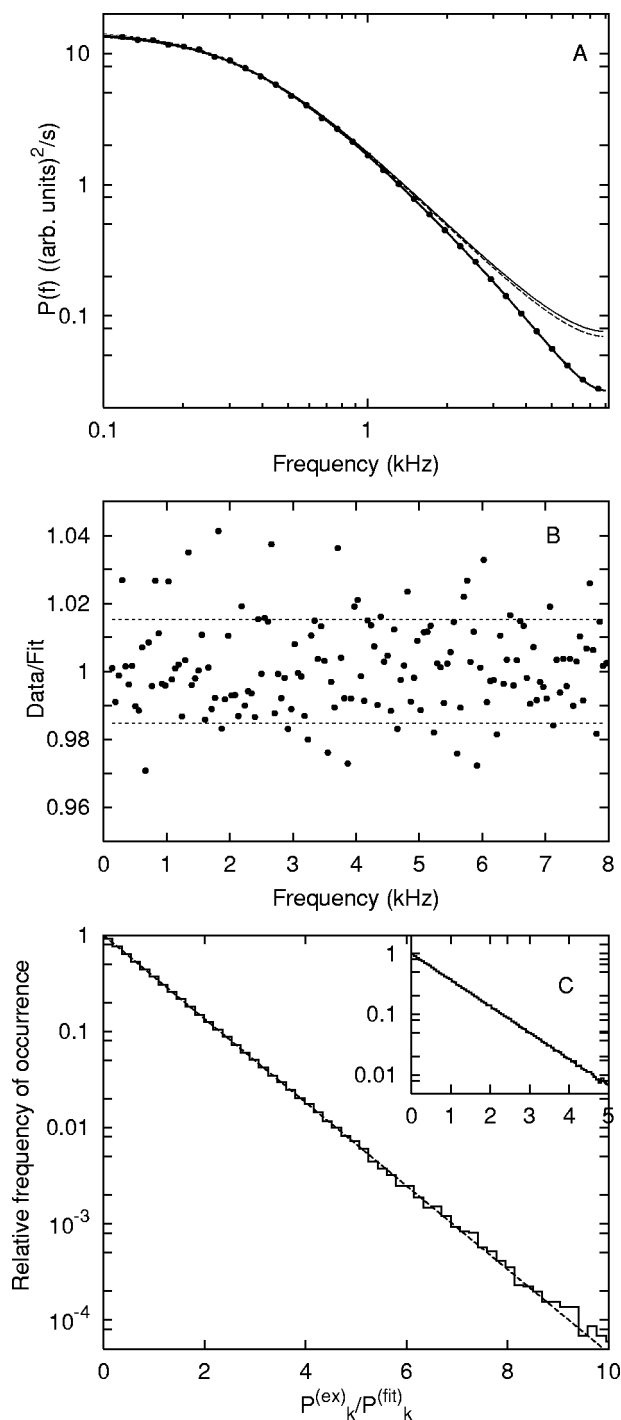


FIG. 5. Same data as in Fig. 2, here fitted with $f_{\max} = f_{\text{Nyq}}$. (a) The thick solid line is the theoretical spectrum in Eq. (34), filtered and aliased, then fitted to the experimental spectrum in the interval [110 Hz, 8 kHz]. Statistical support for the fit is 96% (Refs. 30 and 31). The data points shown were obtained by blocking the experimental spectrum in intervals of equal length on the *logarithmic* axis, and hence are not the same as those shown in (b). Two dashed lines practically on top of the solid line delineate a vertical window of ± 1 standard deviation of Gaussian scatter of data. Thin solid and dashed lines that overshoot the data are aliased Lorentzian and aliased $P_{\text{hydro}}(f; R/\ell)$, respectively, unfiltered, and with same values for D and f_c as those shown by the thick solid line and given in Table II for the x coordinate. They illustrate the importance of filters and the frequency dependence of hydrodynamical friction. (b), (c) See the caption for Fig. 6.

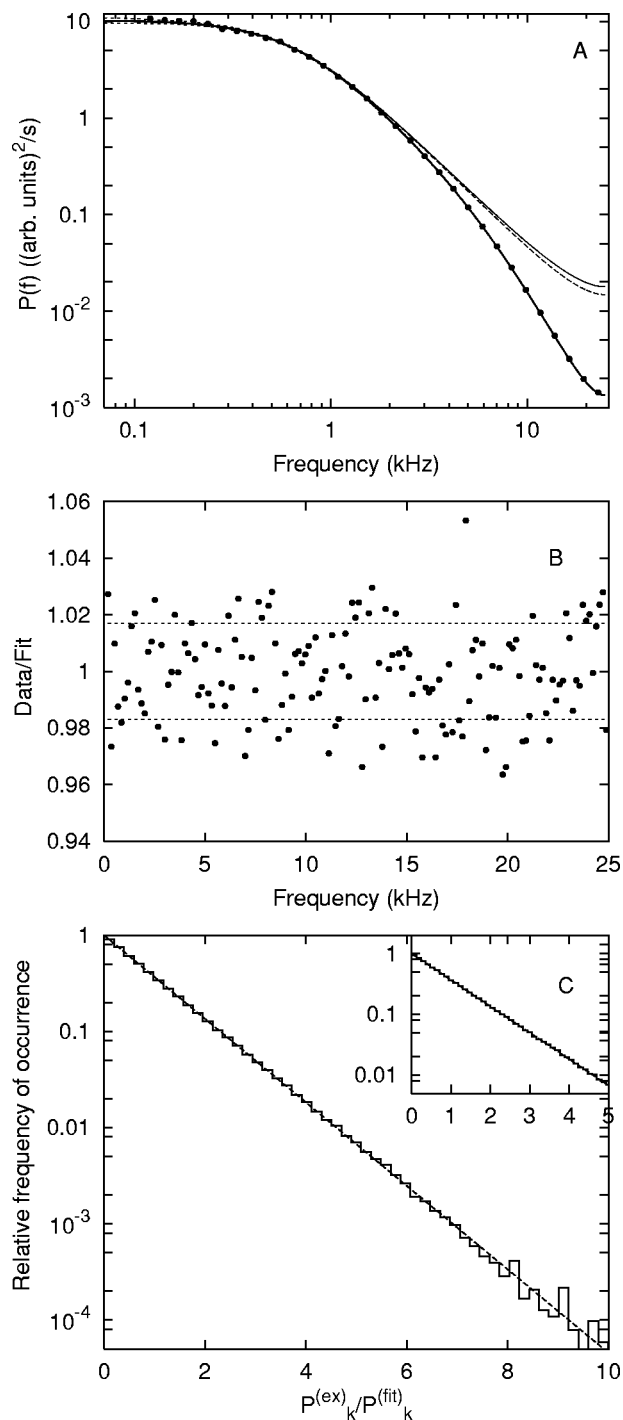


FIG. 6. Same plots as in Fig. 5, but for data obtained with a stronger optical trap and $f_{\text{Nyq}} = 25$ kHz; see the values in Table III. The same power spectral data were used to obtain results given in Table I. Statistical support for the fit is 49% (Refs. 30 and 31). (a) See the caption for Fig. 5. (b) Values of the data fitted to, divided by fitted theory in order to visualize their scatter about a value 1. The two dashed lines delineate the vertical window of ± 1 standard deviation of Gaussian scatter. Thus 68% of the data points should fall between the two dashed lines if the data indeed are Gaussian distributed. They do. Further blocking will reduce the scatter to less than 1%. (c) Histogram of $N = 10^6$ [$N = 1.3 \times 10^6$ in Fig. 5(c)] experimental power-spectral values $P_k^{(\text{ex})}$ measured in units of their expected values P_k , the latter being the fit shown in (a). Inset: Same data binned into a histogram with finer resolution, showing 99% of the data.

TABLE II. Values of fitted parameters for Fig. 5, based on blocking to 150 data points and $f_{\min}=110$ Hz, $f_{\max}=f_{\text{Nyq}}=8$ kHz. $D=0.41$ nm²/μs was used to find the nanometer equivalent for diode output for R_x and R_y . The covariance between f_c and D was -0.95 .

Parameter	x coordinate	y coordinate
f_c (Hz)	374 ± 2	383 ± 2
$f_{3\text{ dB}}^{(\text{diode})}$ (kHz)	6.73 ± 0.17	6.39 ± 0.14
D (arb units) ² /s	610 ± 9	584 ± 8
Arb unit equiv (nm)	26.0 ± 0.2	26.3 ± 0.2
$1 - \alpha^{(\text{diode})2}$	0.92 ± 0.02	0.91 ± 0.01
Support (%)	96	81

equating the value for D obtained in the fit with the value known from Einstein's relation, Eq. (6). Thus, the force $\kappa\Delta x$ exerted at distance Δx from the center of the trap is known to within only 1%–2% error due to calibration of the trap and diode. This error is typically negligible compared to the uncertainty of the position. Thus our calibration scheme essentially eliminates calibration errors from force measurements.

The x coordinate in Table II should be compared with the results in Fig. 2. They were obtained from the same data set. The two values for the corner frequency differ by four standard deviations, with the Lorentzian fit yielding the lower value, because it absorbs the effect of unintentional filtering in this manner, with a small systematic error as result. This point is borne out in Table I and should be compared with Table III's data for the x coordinate obtained from the same data set.

The two values found for $f_{3\text{ dB}}^{(\text{diode})}$ for the x and y coordinates, respectively, are indistinguishable in Table II as well as in Table III. This is what one would expect for a diode with four identical quadrants. It is a coincidence that the values differ only in the fourth digit, not shown in Table III. The two values found for f_c , on the other hand, differ by three to four standard deviations. They differ by 2% (4%), corresponding to an elliptical cross section of the beam with 1% (2%) difference between the lengths of the major and minor axes, or ellipticity of $[1 - (374 \pm 2)/(383 \pm 2)]^{1/2} = 0.15 \pm 0.03$, $\{[1 - (666 \pm 5)/(637 \pm 5)]^{1/2} = 0.21 \pm 0.04\}$. This ellipticity does not differ significantly from the 10% maximum ellipticity of the laser beam promised by the manufacturer. Also, trap ellipticity and laser ellipticity are not necessarily the same thing. Polarized laser beams, even if perfectly nonelliptical, tend to get focused onto elliptical, diffraction limited spots in the image plane. This might be the source of differences between the trap stiffness ellipticity

TABLE III. Values of fitted parameters for Fig. 6, based on fit to 150 blocked data points and $f_{\min}=110$ Hz, $f_{\max}=f_{\text{Nyq}}=25$ kHz. The covariance between f_c and D was -0.95 .

Parameter	x coordinate	y coordinate
f_c (Hz)	666 ± 5	637 ± 5
$f_{3\text{ dB}}^{(\text{diode})}$ (kHz)	7.27 ± 0.04	7.27 ± 0.05
D (arb units) ² /s	447 ± 9	467 ± 9
Arb unit equiv (nm)	30.3 ± 0.3	29.6 ± 0.3
$1 - \alpha^{(\text{diode})2}$	0.928 ± 0.001	0.924 ± 0.001
Support (%)	49	52

one measures and the laser beam ellipticity specified by the manufacturer.

According to theory, the blocked experimental data points are statistically independent and normally distributed with known standard deviations. The “residual plot” in Fig. 5(b) [6(b)] shows the scatter about their expected value, fitted theory, in units of this expected value. Figures 5(b) and 6(b) show that the theoretical power spectrum presented here fits the experimental one perfectly.

Figures 5(c) and 6(c) provide a more radical illustration that the theoretical power spectrum used here really describes the expected value of the experimental spectrum: The “raw” experimental spectral values, i.e., unaveraged and unblocked values, were divided with the fitted theoretical value and binned into histograms that show that the raw experimental spectral values really *are* exponentially distributed about their expected value, as stated by theory. This is a powerful illustration of the correctness of the theory, as well as of the experiment: The histogram shows an exponential distribution over four decades obtained from experimental values that range over no less than seven decades: the four decades they scatter about their expected value, plus the three decades that this expected value varies with the frequency.

XVI. DISCUSSION

A. When precision is no concern

In many biological experiments, e.g., 10%–20% calibration error is of no concern because other sources of error are dominant. So the trapping force can be estimated with sufficient—albeit unknown—precision with the roughest calibration based on a Lorentzian spectrum. Freely available MATLAB software²⁶ will do this as was shown in Sec. IV.

B. When precision is a concern

When precision is a concern an optical trap can advantageously be calibrated as was demonstrated above. Our recommendations—which we have implemented in freely available MATLAB software²⁶—thus are the following.

- When plotting the experimental power spectrum, compress data by blocking to show fewer data points with smaller scatter about their expected value. After all, we know *a priori* that the expected value is a smoothly varying function of the frequency. So the data can advantageously reflect this.
- Plot P_{xy} (defined in Appendix C) and use its minimization as a criterion for good alignment of the diode with the laser beam.
- If P_{xy} cannot be made to vanish, find a linear coordinate transformation to a frame of reference in which it does vanish, and work in this frame of reference.
- The frequency dependence of the friction coefficient and of the Brownian noise should be taken into account. Not only is that correct theory, but using it costs nothing: No new fitting parameters are introduced with it.
- Data acquisition electronics contain antialiasing filters.

Their effect is known, or easily measured with a signal generator, so it costs nothing to account for it when it affects the power spectrum recorded. If the filters are set to have minimal effect, that also minimizes the effect of imprecise knowledge about these filters' parameter values.

- (f) One should be aware that one's position detection system may have frequency-dependent sensitivity, hence may act as an unintended low-pass filter. Ours, a Si PIN diode used with a 1064 nm laser, does, and it is by far the most important filter in our setup. However, since we know the form of its characteristic, we can calibrate its parameters from the very power spectrum we wanted to fit. This is the optimal way in which to determine these parameters, because their values depend on experimental circumstances. If one calibrates with $f_{\max}^2 \ll f_{3\text{ dB}}^2$, one should use the approximation in Eq. (G1). If one uses another kind of quadrant photodiode and/or laser wavelength, this filter effect may be different or absent.^{44,45}
- (g) Aliasing due to finite sampling frequency always occurs, unless one's data acquisition system uses oversampling. Aliasing is easily accounted for, however, and doing so costs nothing if the theory one aliases is also correct at frequencies $f > f_{\text{Nyq}}$ that contribute through aliasing to the spectrum below f_{Nyq} . No new fitting parameters are introduced, only f_{Nyq} , which is known to high precision.
- (h) Leakage,³⁰ on the other hand, is truly negligible because the power spectrum of a trapped bead is a smooth and slowly varying function. So there is no need to introduce window functions that reduce leakage. Consequently, overlapping data windows that compensate for loss of information caused by window functions are also not needed. However, if built into one's data acquisition software, they can be used as they were intended: for quick, on-line data compression. The correlations they introduce in the resulting power spectrum are negligible if a very large number of windows is used.
- (i) The scatter of experimental power spectral values about their expected values is known theoretically. So it costs nothing to use correct error bars, and doing so yields correct stochastic error bars on fitted parameters such as f_c and D , and, last but not least, use of correct error bars makes it possible to obtain statistical support for fits.
- (j) Plots like Figs. 1, 2(b), 5(b) and 5(c), 6(b) and 6(c), and 7–10 are well worth doing. They provide simple, strong, virtually model-independent checks that will catch many kinds of errors in one's experiment and initial data analysis, if present.
- (k) If the fitted value of D is used to calibrate the length scale of displacements measured, one should be aware that the viscosity of the fluid in which one measures may differ significantly from that of pure water at the same temperature. If this is so, reliable calculation or

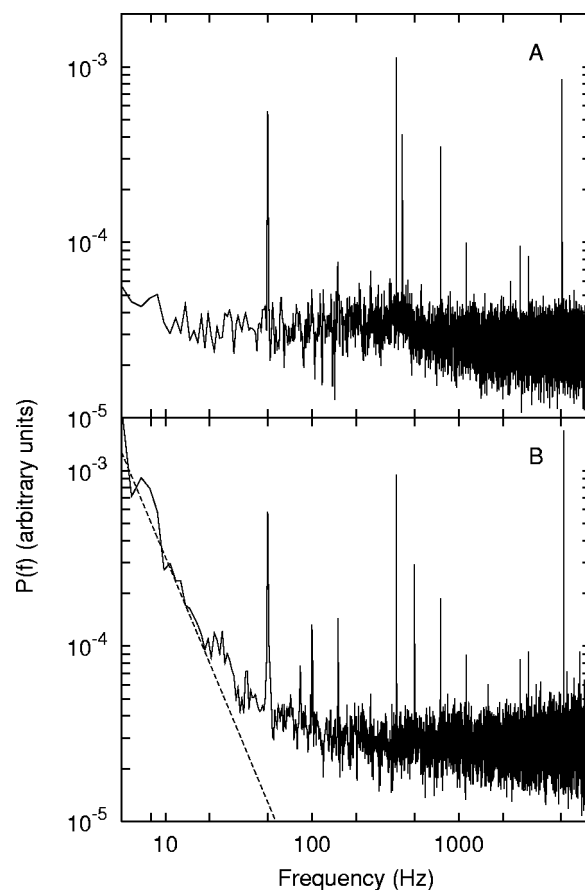


FIG. 7. (a) Dark spectrum: Power spectrum recorded with the diode in total darkness, a measure of the electronic noise level. The spike at 50 Hz is caused by the power supply. All values are a factor of 10^2 – 10^4 below our calibration spectra. (b) Light spectrum: Power spectrum recorded with the trap's laser light impinging directly onto the photodiode with no microsphere in the trap. The dashed line at low frequencies has a slope of -2 .

measurement of its viscosity is needed, or a direct measurement of length scales by moving a fixed bead with a piezo stage.

- (l) Finally, one should beware that the procedure described here calibrates the *center* of the trap. This makes it valid anywhere near the center where the trapping potential is harmonic. That includes everywhere Brownian motion took our bead during calibration, it seems from Fig. 10. How to calibrate off center, at a given displacement along the beam axis, is a separate project of practical interest, but was not addressed here.

ACKNOWLEDGMENTS

This work was prompted by Simon Tolić-Nørrelykke, who wanted to calibrate tweezers in a statistically correct manner. The authors are grateful to Steve Block, Ernst-Ludwig Florin, Joe Howard, and Christoph Schmidt for sharing with them their expertise on tweezers and calibration. The authors also appreciate help with experimental techniques from Jakob Kisbye Dreyer.

APPENDIX A: NOTATION

For convenience, our notation and characteristic values of parameters and variables are given in Table IV.

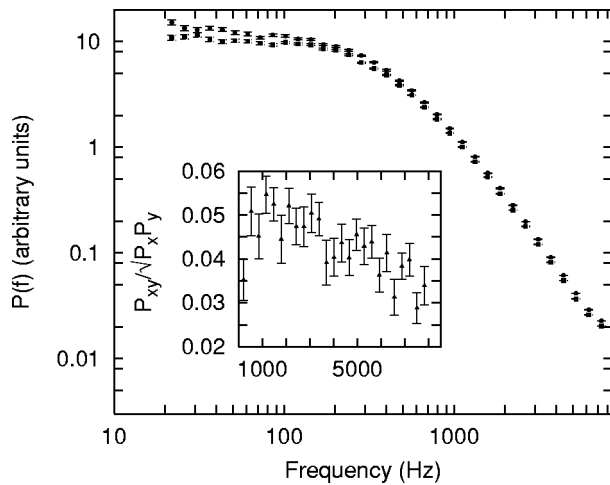


FIG. 8. Experimental power spectra for x and y coordinates (lower and upper data points, respectively). Points plotted here are averages over “blocks” of points from the original power spectrum; see Appendix E. The error bars were calculated from data within blocks. Since the block intervals were chosen to be of equal size on the logarithmic frequency axis used here, the number of data points in a block grows exponentially with the frequency. Consequently, the error bars decrease exponentially with an increase in frequency, and range from small at low frequencies to nondiscernible at intermediate and large frequencies. Inset: Experimental values of the dimensionless cross correlation function $P_{xy}/(P_x P_y)^{1/2}$ introduced in Sec. C 1, as a function of the frequency. (Same power spectral data as in Figs. 2 and 5.)

APPENDIX B: NULL TESTS FOR NOISE

We did two simple null tests of our equipment before we recorded power spectra for the bead in the trap. We recorded a “dark spectrum,” the power spectrum generated when the diode is kept in total darkness; see Fig. 7(a). This is a measurement of the equipment’s electronic noise. We see the spectrum is flat, except for a spike at 50 Hz from the power supply, and at a few higher frequencies, 400 Hz in particular. All values are a factor of 10^2 – 10^4 below that of our calibration spectra, hence noise may contribute from 1% to 10% to the spectra, since amplitudes, not spectra, add up. However, the spikes are so narrow and few in addition to being small

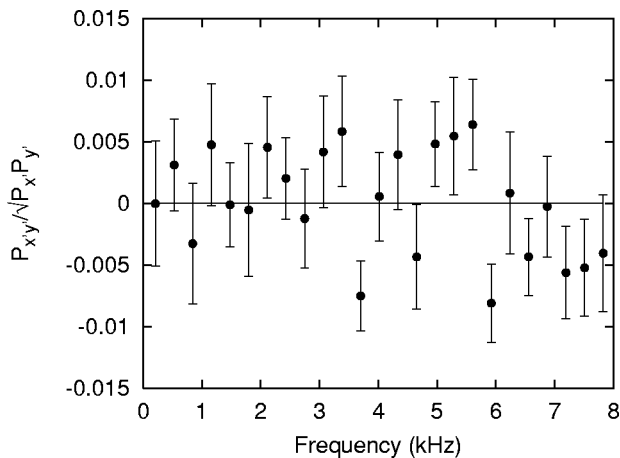


FIG. 9. $P_{x'y'}(f)/[P_x(f)P_y(f)]^{1/2}$ as a function of f at a minimum with respect to (b,c) of $\sum_j P_{x'y'}(f)^2/[P_x(f)P_y(f)]$. Note that the quantity plotted, and hence $P_{x'y'}(f)$, are both zero within errors. More precisely, statistical support for the hypothesis that it vanishes is 10%. (Same data as was used in Figs. 2 and 5.)

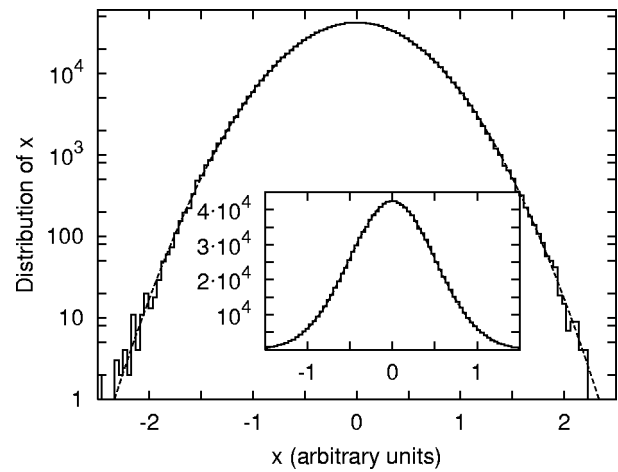


FIG. 10. Linear–log plot of a histogram of the positions that occur in a time series for a bead in a trap. Data are the same as those used in Figs. 2, 8, and 9. Superimposed is the Gaussian distribution with the same second moment as the data. Inset: Linear–linear plot of the same histogram and Gaussian. The 4.5 decades of Gaussian behavior seen here demonstrates that the trap’s potential is harmonic up to $10k_B T$ at least. (Same data as was used in Figs. 2 and 5.)

that they do not matter statistically in our calibration spectra, and also do not show above their noise. The spike at ~ 7 kHz was an exception, but it was so narrow that it easily was filtered out manually and had negligible consequence for the statistics of the calibration spectrum.

We also recorded a “light spectrum,” see Fig. 7(b). Compared with the dark spectrum, this light spectrum shows significant low-frequency noise, plus a peak at 100 Hz, probably caused by stray light. Apart from stray light, the difference is caused by the limited pointing stability of the unscattered laser beam and the optics it passes through relative to the photodiode. The low-frequency noise seems to fall off as f^{-2} , which is what one would observe if the direction of the laser were doing a slow random walk about its average direction driven by white noise.

Although only the microsphere is missing, this light spectrum is not a direct measurement of *all* noise in the system apart from the Brownian noise of the sphere. Mechanical vibrations, e.g., are transmitted to the fluid volume, but not to the light spectrum because the fluid is transparent. They *are*, however, transmitted by the fluid to the sphere’s spectrum when the sphere is present. So this is noise that occurs in the experiment, but not in the light spectrum. Strictly speaking, the light spectrum therefore only provides a lower bound on “all noise but the sphere’s Brownian.” It may nevertheless be a good approximation to all noise, although proof of this is missing.

By choosing $f_{\min}=110$ Hz in calibration fits, we leave low-frequency noise entirely out of the calibration. The light spectrum’s extra features relative to those in Fig. 7(a) above this f_{\min} value all fall a factor of 10^{-4} below the calibration spectrum’s power at the same frequencies, hence add less than 1% to the calibration spectrum.

TABLE IV. Notation used and characteristic values of quantities encountered for data set shown in Figs. 2, 5, and 6. Note: The thermal velocity and the half width of the trap both refer to a single coordinate of motion, i.e., to motion in one dimension.

Quantity	Notation	Equal to	Value (Figs. 2 and 5)	Value (Fig. 6)
Sampling frequency	f_{sample}		16 kHz	50 kHz
Nyquist frequency	f_{Nyq}	$f_{\text{sample}}/2$	8 kHz	25 kHz
Corner frequency	f_c	$\kappa/(2\pi\gamma)$	~ 370 Hz	~ 670 Hz
Frequency where $\delta=R$	f_ν	$\nu/(\pi R^2)$	1.3 MHz	
Frequency of inertial relaxation	f_m	$\gamma/(2\pi m^*) \approx \gamma/(3\pi m)$	1.9 MHz	
Minimum fitted frequency	f_{min}		110 Hz	
Maximum fitted frequency	f_{max}		8 kHz	25 kHz
Diode frequency	$f_{\text{3 dB}}^{(\text{diode})}$		6.8 kHz	7.3 kHz
Total No. of data points	N	$n_w \times 2^{18}$	1.3×10^6	1.0×10^6
Time between measurements	Δt	f_{sample}^{-1}	62.5 μs	20.0 μs
Total duration of measurements	T_{msr}	$N\Delta t$	82 s	21 s
No. of data windows	n_w		5	4
Duration of one data window			16.4 s	5.2 s
Time between windows			1 min	
No. of points of block	n_b		517, 861	869
No. of blocked points	N'		29, 150	150
Diameter of bead	$2R$		1.05 μm	
Density of bead and water	ρ		1.0 g/cm ³	
Mass of bead	m	$4\pi R^3 \rho/3$	6.1×10^{-13} g	
Hydrodynamical mass	m^*	$m + 2\pi R^3 \rho/3$	9.1×10^{-13} g	
Thermal energy	$k_B T$		4.1 pN nm	
Thermal velocity	$\langle v^2 \rangle^{1/2}$	$k_B T/m$	3 mm/s	
Kinematic viscosity	ν		1.0 $\mu\text{m}^2/\mu\text{s}$	
Reynolds number	N_{Re}	$R\langle v^2 \rangle^{1/2}/\nu$	1.4×10^{-3}	
Drag/friction coefficient	γ	$6\pi\rho\nu R$	9×10^{-6} g/s	
Trap stiffness	κ	$2\pi f_c \gamma$	0.021 pN/nm	0.038 pN/nm
Relaxation time in trap	t_{trap}	$\gamma/\kappa = (2\pi f_c)^{-1}$	0.5 ms	0.2 ms
Diffusion coefficient	D	$k_B T/\gamma$	0.41 nm ² /μs	
Inertial time scale	t_{inert}	m/γ	56 ns	
Half width of trap	$\langle x^2 \rangle^{1/2}$	$(k_B T/\kappa)^{1/2}$	14 nm	10 nm
Penetration depth	δ		Frequency dependent	

APPENDIX C: CROSSTALK BETWEEN CHANNELS

1. How to decorrelate channels

The photodiode that we used to measure the bead's position consists of four quadrants, each of which outputs voltage proportional to the amount of light impinging upon it. We number the quadrants I, II, III, and IV like the quadrants of a two-dimensional (2D) coordinate system, and denote their output voltages V_I , V_{II} , V_{III} , and V_{IV} . Then changes in the voltage and the ratios,

$$V_z \equiv V_I + V_{II} + V_{III} + V_{IV}, \quad (\text{C1})$$

$$R_x \equiv (V_I - V_{II} - V_{III} + V_{IV})/V_z, \quad (\text{C2})$$

$$R_y \equiv (V_I + V_{II} - V_{III} - V_{IV})/V_z, \quad (\text{C3})$$

are, to good first approximation,^{35,46–48} proportional to changes in the bead's position (z, x, y), with z the coordinate along the laser beam's axis.

Figure 8 shows that this approximation is not adequate when precision is desired. The experimentally recorded “coordinates” $R_x(t)$ and $R_y(t)$ are not independent. Their power spectra, $P_x(f) \equiv |\hat{R}_x(f)|^2$ and $P_y(f) \equiv |\hat{R}_y(f)|^2$, where the caret denotes discrete Fourier transformation, Eq. (12), are plotted in Fig. 8, together with $P_{xy}(f) \equiv \text{Re}[\hat{R}_x(f)\hat{R}_y^*(f)]$. When x and y are uncorrelated degrees of freedom, so are R_x

and R_y , hence so are \hat{R}_x and \hat{R}_y . Consequently, P_{xy} should vanish compared to P_x and P_y . We find $P_{xy}(f)/[P_x(f)P_y(f)]^{1/2} \approx 3\% - 5\%$, however, as shown in the inset in Fig. 8.

Two explanations for crosstalk given below suggest that (R_x, R_y) is a linear function of (x, y) , and vice versa, and that this function does not depend on time. Assuming this, we look for a linear transformation of (R_x, R_y) to a pair of coordinates (x', y') for which $P_{x'y'} = 0$. If we can find such a transformation, it does not matter what motivated the search for it: the transformed coordinates are the correct Cartesian coordinates in which to analyze the bead's motion and calibrate the trap. To find this transformation, we must find two real constants, b and c , such that the time series,

$$(x'(t), y'(t)) \equiv (R_x(t) + bR_y(t), R_y(t) + cR_x(t)), \quad (\text{C4})$$

has the property that $P_{x'y'}(f) = 0$ for all f .

Clearly, constants b and c are greatly overdetermined. Nevertheless, we were able to find them for all time series that we have analyzed, and have also found that the solution is almost degenerate. This is because $P_x(f)$, $P_y(f)$, and $P_{xy}(f)$ are nearly proportional to each other. It probably also helped that before we recorded any of the data used here, we aligned the diode with the laser beam using as the alignment

criterion $\langle R_x \rangle = \langle R_y \rangle = 0$ and P_{xy} minimal (all three computed and plotted on line).

In general, the transformation just defined gives

$$P_{x'} = P_x + 2bP_{xy} + b^2P_y, \quad (C5)$$

$$P_{y'} = P_y + 2cP_{xy} + c^2P_x, \quad (C6)$$

$$P_{x'y'} = (1 + bc)P_{xy} + cP_x + bP_y. \quad (C7)$$

We found $(b, c) = (0.47, -0.56)$ by minimizing $\sum_f P_{x'y'}(f)^2 / [P_x(f)P_y(f)]$ with respect to b and c . As desired, we found that at the minimum $P_{x'y'}(f) / [P_x(f)P_y(f)]^{1/2} = 0$ was satisfied for all f to within experimental error of this quantity; see Fig. 9.

Having determined b and c in this manner, the resulting power spectra, $P_{x'}$ and $P_{y'}$, for the uncoupled coordinates (x', y') are the spectra that we analyzed in the manner described in the body of this article. So we drop the prime from the notation hereafter, but it should always be understood implicitly.

2. Possible origins of crosstalk

If the parabolic trapping potential V is perfectly rotationally symmetric about the beam axis (chosen as the z axis), $V(x', y', z) = v(x'^2 + y'^2, z)$, the bead's equation of motion decouples no matter which pair of Cartesian coordinates (x', y') we use, as long as they are orthogonal to the beam axis. If the parabolic trap is *not* rotationally symmetric, but elliptic about the beam axis, decoupling is achieved in coordinates (x', y') that coincide with the major and minor axes of the ellipse.

Figure 8 shows that P_x and P_y are approximately proportional to each other: The data set for one function is shifted vertically relative to the data set for the other function by an amount approximately independent of frequency f . This means that the two channels have nearly the same corner frequency. So the trap is nearly rotationally symmetric.

With an asymmetric trap excluded, the simplest explanation for the constant ratio between P_x and P_y is a difference in sensitivity of the photodiode with respect to the two directions. This would come about if the four quadrants of the diode are not identically sensitive, and this would also explain the nonvanishing values for P_{xy} , including its nearly constant ratio to P_x and P_y : R_x becomes linearly correlated with R_y if we introduce independent sensitivities s_i for each of the quadrants, $V_i = s_i L_i$, $i = \text{I, II, III, and IV}$, where L_i is the amount of light impinging on the i th quadrant. If, e.g., a spot of light moves in the x direction, $L_{\text{I}} + L_{\text{II}}$ remains constant, as does $L_{\text{III}} + L_{\text{IV}}$ and V_z . The ratio R_y changes value when $s_{\text{I}} \neq s_{\text{II}}$ and/or $s_{\text{III}} \neq s_{\text{IV}}$, however. Note that such asymmetry needs not be a property of the diode itself. All four quadrants could be identical, but have a nonlinear relationship between input light intensity and output voltage. In that case, less-than-perfect centering of the laser beam on the diode will cause different amounts of light to fall on different quadrants, and hence make them respond with different sensitivity to the small changes in light that correspond to movement of the bead.

Another explanation, which does not exclude the first, could be small asymmetry in the spot of light scattered by the bead onto the photodiode. That would cause different amounts of light to shift between quadrants for identical shifts of the bead in the x and y directions. If, furthermore, some of that asymmetrically scattered light falls beyond the edge of the quadrant diode, then a shift of the bead in the x direction will change R_y , and hence register as a correlated change in y .

APPENDIX D: MODEL-INDEPENDENT DATA ANALYSIS

Histograms of x and y positions of the decorrelated time series were consistent with a harmonic trapping potential up to $10 k_B T$, at least, as shown in Fig. 10 for the x channel.

The parabola through the data in the lin-log plot shows that the data are modeled well with $V(x) = \frac{1}{2} \kappa x^2$ in the range of x values visited. It is very satisfying that a model-independent data analysis can point so precisely to a specific model. If we determined the value of κ in this manner, however, we may find too low a value. This is because the true distribution $\propto \exp[-V(x)/k_B T]$ was smeared to a wider one by low-frequency vibrations which are external to the experiment in the sense that they do not originate in the bead's thermal motion. We may also find too large a value for κ because low-pass frequency filters artificially narrow the distribution of positions recorded. Furthermore, since fits like that in Fig. 10 do not calibrate the position detection system, the units for x and y remain arbitrary until an independent calibration of the position detection system is carried out, e.g., by finding f_c . Force measurements would consequently contain errors that originate in that calibration as well, were we to do one.

APPENDIX E: MAXIMUM-LIKELIHOOD FITTING AND DATA COMPRESSION

Suppose we data compress a power spectrum by blocking, and only then fit to it. How should that be done, and what is the approximation introduced by this?

In an unprocessed (uncompressed) power spectrum, the power spectral values are *exponentially* distributed. Least-squares fitting presupposes that the data are Gaussian distributed. With sufficient compression, a spectrum whose values were exponentially distributed will turn into a spectrum with much less scatter and Gaussian distributed values by virtue of the central limit theorem. So after compression, least-squares fitting can be applied. What is the approximation involved, we should ask, and what is the precision to expect, we *must* ask, in view of the precision we achieve in calibrating to compressed spectra, and hence want to claim for the calibration method described.

In order to answer these questions, we first observe that maximum-likelihood fitting to exponentially distributed data is equivalent to minimizing

$$\mathcal{F} \equiv -\log p = \sum_k (P_k^{(\text{ex})}/P_k + \log P_k). \quad (E1)$$

Now consider the contribution from one block of data to \mathcal{F} in Eq. (E1) before blocking has been done,

$$\Delta\mathcal{F}(\text{block}) = \sum_{f \in \text{block}} \left(\frac{P^{(\text{ex})}(f)}{P(f)} + \log P(f) \right). \quad (\text{E2})$$

In this equation we expand $P(f)$ at $f = \bar{f}$ to second order in $f - \bar{f}$, and find

$$\Delta\mathcal{F}(\text{block}) = n_b \left[\frac{\bar{P}^{(\text{ex})}(\bar{f})}{P(\bar{f})} + \log P(\bar{f}) - \frac{1}{24} \left(\frac{n_b \Delta f P'(\bar{f})}{P(\bar{f})} \right)^2 \right], \quad (\text{E3})$$

where the last term on the right-hand side was obtained by replacing the sum $\sum_{f \in \text{block}}$ with an integral over f between $\bar{f} \pm \frac{1}{2} n_b \Delta f$.

Note that $n_b \Delta f P'(\bar{f})/P(\bar{f})$ is the relative change in $P(f)$ across a block. Since $\Delta f = 1/T = 0.06$ Hz while $P'(f)/P(f) = \mathcal{O}(f_c^{-1})$, it is possible to choose n_b large, e.g., $n_b = 500$, and still have the last term in Eq. (E3) negligible, so that we are left with the same form as Eq. (E1) for maximum-likelihood estimation of the theory's parameters from given, now blocked, experimental data.

Calculation entirely like the one leading from Eqs. (E2)–(E3) shows that the expected value and RMSD for $\bar{P}^{(\text{ex})}(\bar{f})$ are

$$\langle \bar{P}^{(\text{ex})}(\bar{f}) \rangle = P(\bar{f}), \quad (\text{E4})$$

$$\sigma[\bar{P}^{(\text{ex})}(\bar{f})] = \sigma[P^{(\text{ex})}(\bar{f})]/\sqrt{n_b} = P(\bar{f})/\sqrt{n_b}, \quad (\text{E5})$$

to the orders in $n_b \Delta f$ given. In this last identity, Eq. (E5), if the power spectrum blocked was already windowed, its values were not exponentially distributed, and n_b should be replaced with $n_w n_b$ in the case of nonoverlapping rectangular windows, and with $9 n_w n_b / 11$ in the case of Hanning windows (Ref. 30, p. 428).

For large n_b , or, if $n_w \neq 1$, for large $n_w n_b$, the central limit theorem tells us that $\bar{P}^{(\text{ex})}(\bar{f})$ is Gaussian distributed with the expected value and root-mean-square deviations given in Eqs. (E4) and (E5). Fitting to data that are known to be Gaussian distributed is usually done with the method of least squares. So it is natural to ask how the method of least squares relates to the maximum-likelihood estimation discussed above. According to Eq. (E3) with its last term neglected, maximum-likelihood estimation based on blocked data amounts to minimization of

$$\bar{\mathcal{F}} \equiv n_b \sum_{\bar{f}} \left(\frac{\bar{P}^{(\text{ex})}(\bar{f})}{P(\bar{f})} + \log P(\bar{f}) \right). \quad (\text{E6})$$

A brief calculation shows that this is equivalent to minimization of

$$\bar{\mathcal{F}}_2 \equiv \frac{1}{2} \chi^2 + \sum_{\bar{f}} \log P(\bar{f}), \quad (\text{E7})$$

where

$$\chi^2 \equiv n_b \sum_{\bar{f}} \left(\frac{\bar{P}^{(\text{ex})}(\bar{f}) - P(\bar{f})}{P(\bar{f})} \right)^2. \quad (\text{E8})$$

$\bar{\mathcal{F}}_2$ is precisely the expression one must minimize with respect to fitting parameters in the function P when these parameters are maximum likelihood estimated from a set of experimental data $[\bar{f}, \bar{P}^{(\text{ex})}(\bar{f})]_{\bar{f}, \dots}$, that are normally distributed with the theoretical expected value and root-mean-square deviation given in Eqs. (E4) and (E5).

Thus we see that maximum-likelihood estimation of P simplifies to χ^2 minimization only when n_b is so large that one can ignore the last term in Eq. (E7) compared to the first. This last term occurs because our theory gives both the expected value for the data *and* the data's root-mean-square deviation for this expected value. Thus the parameters of our theory occur also in the root-mean-square deviation, the logarithm of which is the second term in $\bar{\mathcal{F}}_2$ above. In textbook derivations of ordinary least-squares fitting, this term is independent of the fitted theory's parameters, e.g., because experimentally measured error bars are used, hence only the first term, χ^2 , is minimized.

Since $n_b n_w$ ranged from 2500 to 4350 in our data analysis, we could neglect the second term in $\bar{\mathcal{F}}_2$ relative to the first term, and fit by minimizing only χ^2 . Factors other than this approximation limited our precision. However, with data and equipment other than those discussed here, we have encountered situations where χ^2 fitting clearly was not adequate, and we had to minimize the full expression for $\bar{\mathcal{F}}_2$.⁴⁴

APPENDIX F: CALCULATION OF $\sigma(f_c)$

Equations (25) and (27) give f_c as a function of the experimental power spectrum $(P_k^{(\text{ex})})_{k=1, \dots, N'}$. Since $P_k^{(\text{ex})}$ is a random variable, so is the value we find for f_c . We determine $\sigma(f_c)$ by the usual method of linear propagation of errors. The calculation is long, but is simplified by a convenient choice of notation.

$$\sigma^2(f_c^2) = \sum_{k=1}^{N'} \left(\frac{\partial f_c^2}{\partial P_k^{(\text{ex})}} \right)_{P^{(\text{ex})}=P}^2 \sigma^2(P_k^{(\text{ex})}), \quad (\text{F1})$$

$$\frac{\partial f_c^2}{\partial P_k^{(\text{ex})}} = \sum_{p,q} \frac{\partial f_c^2}{\partial S_{p,q}} \frac{\partial S_{p,q}}{\partial P_k^{(\text{ex})}}, \quad (\text{F2})$$

$$\frac{\partial S_{p,q}}{\partial P_k^{(\text{ex})}} = q f_k^{2p} P_k^{(\text{ex})q-1}, \quad (\text{F3})$$

$$f_c^2 = \mathcal{N}/\mathcal{D}, \quad (\text{F4})$$

where we have introduced an explicit notation for the numerator and the denominator,

$$\mathcal{N} \equiv S_{0,1} S_{2,2} - S_{1,1} S_{1,2}, \quad (\text{F5})$$

$$\mathcal{D} \equiv S_{0,2} S_{1,1} - S_{0,1} S_{1,2}. \quad (\text{F6})$$

Then

$$\frac{\partial f_c^2}{\partial S_{p,q}} = \mathcal{D}^{-1} \left(\frac{\partial \mathcal{N}}{\partial S_{p,q}} - f_c^2 \frac{\partial \mathcal{D}}{\partial S_{p,q}} \right), \quad (\text{F7})$$

and thus

$$\begin{aligned} \frac{\partial f_c^2}{\partial P_k^{(\text{ex})}} = \mathcal{D}^{-1} & (\check{S}_{2,2} - \check{S}_{1,2}(f_c^2 + f_k^2) - 2\check{S}_{1,1}(f_c^2 + f_k^2)P_k^{(\text{ex})} \\ & + 2\check{S}_{0,1}(f_c^2 + f_k^2)^2 P_k^{(\text{ex})}), \end{aligned} \quad (\text{F8})$$

where we have introduced the notation,

$$\check{S}_{p,q} \equiv \sum_{k=1}^{N'} (f_c^2 + f_k^2)^p P_k^{(\text{ex})q}, \quad (\text{F9})$$

and note that $\check{S}_{0,q} = S_{0,q}$, and $S_{0,0} = N'$. In this notation,

$$\mathcal{D} = \check{S}_{0,2}\check{S}_{1,1} - \check{S}_{0,1}\check{S}_{1,2}. \quad (\text{F10})$$

Evaluated at

$$P_k^{(\text{ex})} = P_k = b^{-1}(f_c^2 + f_k^2)^{-1}, \quad (\text{F11})$$

$$\check{S}_{p,q} = b^{-q}\check{S}_{p-q,0}, \quad (\text{F12})$$

and consequently,

$$\left(\frac{\partial f_c^2}{\partial P_k^{(\text{ex})}} \right)_{P^{(\text{ex})}=P} = b^{-2}\mathcal{D}^{-1}(\check{S}_{-1,0}(f_c^2 + f_k^2) - \check{S}_{0,0}), \quad (\text{F13})$$

with

$$\mathcal{D}(P^{(\text{ex})}=P) = b^{-3}(\check{S}_{-2,0}\check{S}_{0,0} - \check{S}_{-1,0}^2). \quad (\text{F14})$$

Using

$$\sigma(P_k^{(\text{ex})}) = \eta_b^{-1/2}P_k = n_b^{-(1/2)}b^{-1}(f_c^2 + f_k^2)^{-1} \quad (\text{F15})$$

(n_b should be replaced with $n_b n_w$ if $n_w \neq 1$), we find

$$\begin{aligned} \sigma^2(f_c^2) &= n_b^{-1}b^{-6}\mathcal{D}^{-2}\check{S}_{0,0}(\check{S}_{-2,0}\check{S}_{0,0} - \check{S}_{-1,0}^2), \\ &= n_b^{-1}b^{-3}\mathcal{D}^{-1}\check{S}_{0,0}, \\ &= \frac{\check{S}_{0,0}}{n_b(\check{S}_{-2,0}\check{S}_{0,0} - \check{S}_{-1,0}^2)}. \end{aligned} \quad (\text{F16})$$

Finally, we replace the sums with the integrals they approximate,

$$\check{S}_{p,0} = \sum_{k=1}^{N/n_b} (f_c^2 + f_k^2)^p = \frac{T}{n_b} \int_{f_{\min}}^{f_{\max}} df (f_c^2 + f^2)^p \quad (\text{F17})$$

and have, with $x_{\min} \equiv f_{\min}/f_c$ and $x_{\max} \equiv f_{\max}/f_c$,

$$\check{S}_{0,0} = \frac{Tf_c}{n_b} (x_{\max} - x_{\min}), \quad (\text{F18})$$

$$\check{S}_{-1,0} = \frac{T}{n_b f_c} \arctan \left(\frac{x_{\max} - x_{\min}}{1 + x_{\max} x_{\min}} \right), \quad (\text{F19})$$

$$\begin{aligned} \check{S}_{-2,0} &= \frac{T}{2n_b f_c^3} \left[\frac{x_{\max}}{1 + x_{\max}^2} - \frac{x_{\min}}{1 + x_{\min}^2} \right. \\ &\quad \left. + \arctan \left(\frac{x_{\max} - x_{\min}}{1 + x_{\max} x_{\min}} \right) \right], \end{aligned} \quad (\text{F20})$$

from which Eq. (25) follows, when using

$$\frac{\sigma(f_c)}{f_c} = \left(\frac{\sigma^2(f_c^2)}{4f_c^4} \right)^{1/2}. \quad (\text{F21})$$

APPENDIX G: FITTING $f_{3\text{ dB}}^{(\text{diode})}$ AND $\alpha^{(\text{diode})}$

The fit shown in Fig. 5 gives $f_c = 0.37$ kHz and $f_{3\text{ dB}}^{(\text{diode})} = 6.8$ kHz, i.e., the latter is 19 times larger than the former. So the values of these two frequencies are sensitive to different parts of the power spectrum. This does not mean that the covariances between f_c , on the one hand, and $f_{3\text{ dB}}^{(\text{diode})}$ and $\alpha^{(\text{diode})}$ on the other, are negligible. Both f_c and $f_{3\text{ dB}}^{(\text{diode})}$, for example, depend on a large range of frequencies, and consequently have significant covariance for realistic values of both. This is seen when fitting using a program that gives correlations, and can also be shown analytically for a Lorentzian fit with $f_c \ll f_{\max} \lesssim f_{3\text{ dB}}^{(\text{diode})} \ll f_{\text{Nyq}}$ in a calculation analogous to the one done in Appendix F; see Sec. G 1 below. In units of $\sigma(f_c)\sigma(f_{3\text{ dB}}^{(\text{diode,eff})})$, one finds that the covariance of f_c and $f_{3\text{ dB}}^{(\text{diode,eff})}$ is $-2(f_c/f_{3\text{ dB}}^{(\text{diode,eff})})^{1/2}$, which takes values of -0.46 and -0.47 for the values of f_c and $f_{3\text{ dB}}^{(\text{diode,eff})}$ that we found above (Fig. 5, Table II) for the x and the y coordinates, respectively. In view of the approximation involved, this is in good agreement with the values of -0.55 and -0.54 found by the fitting program for the covariance between f_c and $f_{3\text{ dB}}^{(\text{diode})}$ in units of $\sigma(f_c)\sigma(f_{3\text{ dB}}^{(\text{diode})})$. The agreement is even better for the data set whose x -coordinate data are shown in Fig. 6. The fit shown there and the equivalent one for the y coordinate give -0.56 , respectively, -0.55 , for the correlation between f_c and $f_{3\text{ dB}}^{(\text{diode})}$ in units of $\sigma(f_c)\sigma(f_{3\text{ dB}}^{(\text{diode})})$. This compares very well with the analytical result $-2(f_c/f_{3\text{ dB}}^{(\text{diode,eff})})^{1/2} = -0.59$, respectively, -0.58 , for the covariance between f_c and $f_{3\text{ dB}}^{(\text{diode,eff})}$ in units of $\sigma(f_c)\sigma(f_{3\text{ dB}}^{(\text{diode,eff})})$.

Since the covariance in units of $\sigma(f_c)\sigma(f_{3\text{ dB}}^{(\text{diode,eff})})$ is $-2(f_c/f_{3\text{ dB}}^{(\text{diode,eff})})^{1/2}$ in our analytical case based on Lorentzians, we see that one needs an unrealistically small ratio for $f_c/f_{3\text{ dB}}^{(\text{diode})}$ in order to have negligible covariance between these two parameters. We also see that because of their substantial covariance one cannot determine one correctly without determining the other with similar precision. Because of our rich data and well-fitting theory, we determine both f_c and $f_{3\text{ dB}}^{(\text{diode})}$ with the high precision listed in Tables II and III. This precision refers to the 68% probability interval for the parameter in question, with the values for the other three parameters floating; i.e., it is the most conservative, largest interval. So our procedure is quite sound despite the nonvanishing covariance of f_c with $f_{3\text{ dB}}^{(\text{diode})}$.

1. Low-frequency approximation for the diode characteristic function

From Tables II and III we see that less than 10% of the power in the spectrum, $\alpha^{(\text{diode})2}$, is unaffected by the finite response time of the diode. In this case, and for frequencies f for which $(f/f_{3\text{ dB}}^{(\text{diode})})^2 \ll 1$, we have

$$\frac{P(f)}{P_0(f)} = \frac{1 + \alpha^{(\text{diode})2} (f/f_{3\text{ dB}}^{(\text{diode})})^2}{1 + (f/f_{3\text{ dB}}^{(\text{diode})})^2}, \quad (\text{G1})$$

$$\approx \frac{1}{1 + (f/f_{3\text{ dB}}^{(\text{diode, eff})})^2},$$

where we have introduced

$$f_{3\text{ dB}}^{(\text{diode, eff})} \equiv (1 - \alpha^{(\text{diode})2})^{-1/2} f_{3\text{ dB}}^{(\text{diode})}. \quad (\text{G2})$$

The last expression in Eq. (G1) is a simple Lorentzian. Equation (G2) shows that in this case $\alpha^{(\text{diode})}$ combines with $f_{3\text{ dB}}^{(\text{diode})}$ into a single parameter, $f_{3\text{ dB}}^{(\text{diode, eff})}$, an effective 3 dB frequency of a first-order filter that describes the diode's characteristics.

One can use this approximation in a calculation analogous to the one done in Appendix F to obtain the analytical result used above: the covariance of f_c and $f_{3\text{ dB}}^{(\text{diode, eff})}$, in units of $\sigma(f_c)\sigma(f_{3\text{ dB}}^{(\text{diode, eff})})$, is $-2(f_c/f_{3\text{ dB}}^{(\text{diode, eff})})^{1/2}$.

APPENDIX H: ALIASING AND ANTIALIASING

1. What aliasing is

When a signal is sampled at discrete times, t_j , with frequency f_{sample} , the sampling process cannot distinguish frequency components of the signal which differ from each other by integer multiples of the sampling frequency. They all add up to a single amplitude. This is seen as follows: Our experiment records a time series $(x_j)_{j=1,\dots,N}$ by sampling the continuous signal $x(t)$ with frequency f_{sample} for time T_{msr} . With \tilde{x}_k the continuous Fourier transformed in Eq. (7), the continuous signal can be written in terms of its inverse Fourier transform,

$$x(t) = \frac{1}{T_{\text{msr}}} \sum_{n=-\infty}^{\infty} e^{-i2\pi kt/N} \tilde{x}_k. \quad (\text{H1})$$

Inserting this in the *discrete* Fourier transform of our recorded time series, Eq. (12), and using

$$\frac{1}{N} \sum_{j=1}^N e^{i2\pi j(k-\ell)/N} = \sum_{n=-\infty}^{\infty} \delta_{k-\ell, nN}, \quad (\text{H2})$$

where the right-hand side is equal to 1 for $k=\ell$ modulo N , and 0 otherwise, we find

$$\hat{x}_k = \sum_{n=-\infty}^{\infty} \tilde{x}_{k+nN}. \quad (\text{H3})$$

Here the real and imaginary parts of \tilde{x}_{k+nN} are uncorrelated random Gaussian variables with zero mean and common variance in both the Einstein–Ornstein–Uhlenbeck theory and the hydrodynamically correct theory, and for filtered versions of both theories. Hence, so are the real and imaginary parts of \hat{x}_k . Consequently,

$$P_k^{(\text{ex, aliased})} \equiv |\hat{x}_k|^2 / T_{\text{msr}} \quad (\text{H4})$$

is exponentially distributed on the real, non-negative numbers, with mean

$$P_k^{(\text{aliased})} = \langle |\hat{x}_k|^2 \rangle / T_{\text{msr}},$$

$$= \sum_{n=-\infty}^{\infty} \langle |\tilde{x}_{k+nN}|^2 \rangle / T_{\text{msr}},$$

$$= \sum_{n=-\infty}^{\infty} P_{k+nN}. \quad (\text{H5})$$

$P^{(\text{aliased})}$ is obviously a periodic function of k with period N , i.e., of f_k with period f_{sample} . So it is sufficient to know its value in the interval $[-f_{\text{Nyq}}, f_{\text{Nyq}}]$, $f_{\text{Nyq}} = f_{\text{sample}}/2$.

On the other hand, Eq. (H5) shows that neither f_{Nyq} nor f_{sample} represents a sharp frequency cutoff. The value of $P_k^{(\text{aliased})}$ depends through $P_{k+nN}^{(\text{unaliased})}$, $n = \pm 1, \pm 2, \dots$, on frequency components \tilde{x}_k of the signal $x(t)$ outside $[-f_{\text{Nyq}}, f_{\text{Nyq}}]$.

2. Example: Aliased Lorentzian

As a specific example, we consider the Lorentzian, for which

$$P_k^{(\text{aliased})} = \sum_{n=-\infty}^{\infty} \frac{D/(2\pi^2)}{f_c^2 + (f_k + nf_{\text{sample}})^2}$$

$$= \frac{(\Delta x)^2 \Delta t}{1 + c^2 - 2c \cos(2\pi k/N)}. \quad (\text{H6})$$

In the case of $f_c \ll f < f_{\text{Nyq}}$, $P(f) \propto 1/f^2$, hence

$$P_{N/2}^{(\text{aliased})} \propto \sum_{n=-\infty}^{\infty} \frac{1}{(f_{\text{Nyq}} + 2nf_{\text{Nyq}})^2},$$

$$= \frac{2}{f_{\text{Nyq}}^2} \left(1 + \frac{1}{9} + \frac{1}{25} + \frac{1}{49} + \frac{1}{81} + \dots \right)$$

$$\approx \frac{2.47}{f_{\text{Nyq}}^2}, \quad (\text{H7})$$

i.e., aliasing adds almost 150% to the power spectrum near f_{Nyq} . This means that frequencies several times f_{Nyq} contribute significantly to the power spectrum near f_{Nyq} , no matter what value f_{Nyq} has, and one must consequently consider whether the model yielding the Lorentzian really is also valid at these higher frequencies, even if the model is known to be valid below f_{Nyq} .

3. What antialiasing is

Data acquisition electronics have built-in *antialiasing* filters. These filters prevent aliasing of electronic noise from much higher frequencies. However, if not all 3 dB frequencies of these filters are much larger than our highest frequency of interest, the power spectrum we *want* to measure is distorted by antialiasing. Since $f_{3\text{ dB}} = f_{\text{Nyq}}$ is a popular choice, this distortion commonly occurs and is significant; see Fig. 11.

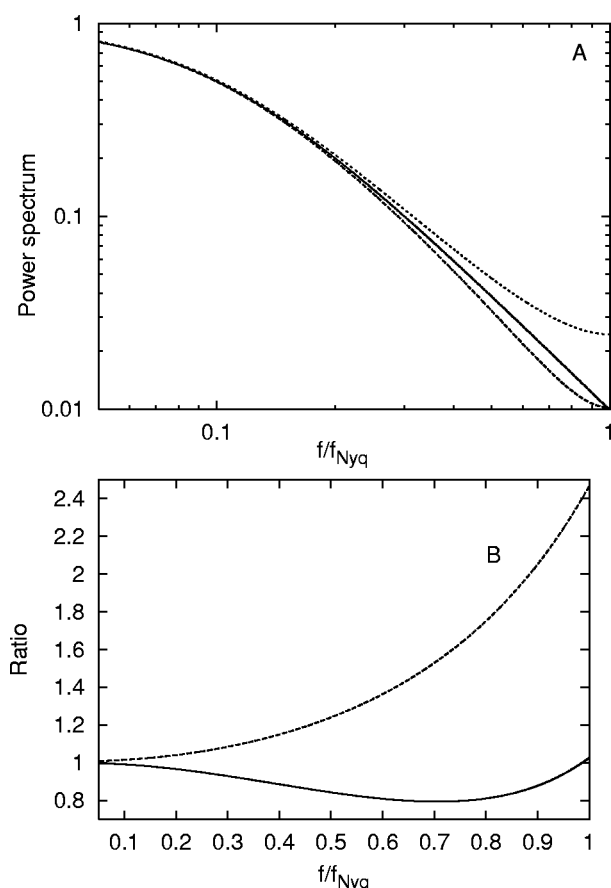


FIG. 11. (a) Solid line: Simple Lorentzian power spectrum with $f_c = 374$ Hz. Dotted line above the Lorentzian: Same simple Lorentzian, but aliased as if the signal were sampled at finite rate $f_{sample} = 2f_{Nyq}$, hence a periodic function with period f_{sample} . Dashed line below the Lorentzian: Same simple Lorentzian, but filtered with a first-order filter with $f_{3dB} = f_{Nyq}$, then aliased as if the signal were sampled at finite rate $f_{sample} = 2f_{Nyq}$. Note that the antialiasing filter with $f_{3dB} = f_{Nyq}$ does not prevent aliasing as such, it only suppresses large frequencies, so less power is aliased. (b) Dashed line: Ratio between the aliased Lorentzian and the simple Lorentzian, i.e., the ratio between power spectra of signals recorded with a finite sampling rate and recorded continuously. Solid line: Ratio between the filtered, aliased Lorentzian, and simple Lorentzian, i.e., the ratio between power spectra of the signal recorded with a finite sampling rate after filtering and recorded continuously with no filtering. Note that the antialiased spectrum falls up to 20% below the unaliased spectrum: Antialiasing filters are for electronic noise suppression, and are no substitute for a correct description of the aliasing caused by the finite sampling time.

It should be avoided when possible by choosing high values for f_{3dB} . Electronic noise *must* be filtered away, but this should be done with minimal effect on the information-containing part of the power spectrum. Although any antialiasing filter is easily accounted for in principle when its characteristic function is known, in practice parameter values of the characteristic function are not known with precision. However, if the filter settings are chosen to minimize filtering, the uncertainty that this lack of precision causes, appears on subdominant digits that describe an already small effect. So this lack of precision may not matter.

4. What antialiasing is not

Antialiasing filters are no substitute for a correct description of the aliasing caused by finite sampling time, as Fig. 11

illustrates: If the theoretical power spectrum for a system is a simple Lorentzian, but the signal from this system is sampled at a finite rate, an aliased Lorentzian results. This is then what one should fit to the experimental spectrum. If one filters the signal before sampling it, say, with $f_{3dB} = f_{Nyq}$, that should also be accounted for. However, one should *not* assume that the filter prevents the aliasing caused by finite sampling time, and then fit a simple Lorentzian to the spectrum of the filtered, sampled signal, to frequencies up to f_{Nyq} . Not if 20% error matters, because the two spectra differ by that much for $0.6f_{Nyq} < f < 0.8f_{Nyq}$. If one fits only to frequencies below $f_{max} = 0.6f_{Nyq}$, a simple Lorentzian is about as bad an approximation to the filtered time series as to the unfiltered one. So in this range also is antialiasing no substitute for a theory that accounts for filters and sampling rates.

- ¹ A. Ashkin, Proc. Natl. Acad. Sci. U.S.A. **94**, 4853 (1997).
- ² S. M. Block, Nature (London) **386**, 217 (1997).
- ³ A. D. Mehta, M. Rief, J. A. Spudich, D. A. Smith, and R. M. Simmons, Science **283**, 1689 (1999).
- ⁴ S. B. Smith, Y. Cui, and C. Bustamante, Science **271**, 795 (1996).
- ⁵ R. G. Larson, T. T. Perkins, D. E. Smith, and S. Chu, Phys. Rev. E **55**, 1794 (1997).
- ⁶ M. S. Z. Kellermayer, S. B. Smith, H. L. Granzier, and C. Bustamante, Science **276**, 1112 (1997).
- ⁷ M. D. Wang, H. Yin, R. Landick, J. Gelles, and S. M. Block, Biophys. J. **72**, 1335 (1997).
- ⁸ M. W. Berns, Sci. Am. **April**, 52 (1998).
- ⁹ M. D. Wang, M. J. Schnitzer, H. Yin, R. Landick, J. Gelles, and S. M. Block, Science **282**, 902 (1998).
- ¹⁰ C. Veigel, M. L. Bartoo, D. C. S. White, J. C. Sparrow, and J. E. Molloy, Biophys. J. **75**, 1424 (1998).
- ¹¹ K. Visscher, M. J. Schnitzer, and S. M. Block, Nature (London) **400**, 184 (1999).
- ¹² B. Schnurr, F. Gittes, F. C. MacKintosh, and C. F. Schmidt, Macromolecules **30**, 7781 (1997).
- ¹³ F. Gittes, B. Schnurr, P. D. Olmsted, F. C. MacKintosh, and C. F. Schmidt, Phys. Rev. Lett. **79**, 3286 (1997).
- ¹⁴ I. M. Tolić-Nørrellykke, E.-L. Munteanu, G. Thon, L. Oddershede, and K. Berg-Sørensen, (unpublished).
- ¹⁵ A. Pralle, E.-L. Florin, E. H. K. Stelzer, and J. K. H. Hörber, Appl. Phys. A: Mater. Sci. Process. **A66**, S71 (1998).
- ¹⁶ L. Oddershede, H. Flyvbjerg, and K. Berg-Sørensen, J. Phys.: Condens. Matter **15**, S1737 (2003).
- ¹⁷ K. Berg-Sørensen, L. Oddershede, and H. Flyvbjerg, Proc. SPIE (to be published).
- ¹⁸ T. Tlusty, A. Meller, and R. Bar-Ziv, Phys. Rev. Lett. **81**, 1738 (1998).
- ¹⁹ K. Svoboda and S. M. Block, Annu. Rev. Biophys. Biomol. Struct. **23**, 247 (1994).
- ²⁰ R. M. Simmons, J. T. Finer, S. Chu, and J. A. Spudich, Biophys. J. **70**, 1813 (1996).
- ²¹ K. Visscher and S. M. Block, Methods Enzymol. **298**, 460 (1998).
- ²² F. Gittes and C. F. Schmidt, Methods Cell Biol. **55**, 129 (1998).
- ²³ E.-L. Florin, A. Pralle, E. H. K. Stelzer, and J. K. H. Hörber, Appl. Phys. A: Mater. Sci. Process. **A66**, S75 (1998).
- ²⁴ W. Singer, S. Bernet, N. Hecker, and M. Ritsch-Marte, J. Mod. Opt. **47**, 2921 (2000).
- ²⁵ M. Capitanio, G. Romano, R. Ballerini, M. Giuntini, F. C. Pavone, D. Dunlap, and L. Finzi, Rev. Sci. Instrum. **73**, 1687 (2002).
- ²⁶ I. M. Tolić-Nørrellykke, K. Berg-Sørensen, and H. Flyvbjerg, Comput. Phys. Commun. (to be published).
- ²⁷ L. Oddershede, S. Grego, S. F. Nørrellykke, and K. Berg-Sørensen, Probe Microsc. **2**, 129 (2001).
- ²⁸ A. Jones, Customer Service, Bangs Laboratories, Inc., 9025 Technology Drive, Fishers, IN 46038-2886; private communication (2002).
- ²⁹ R. Kubo, M. Toda, and N. Hashitsume, Statistical Physics (Springer, Heidelberg, 1985), Vol. 2.
- ³⁰ W. H. Press, B. P. Flannery, S. A. Teukolsky, and W. T. Vetterling, Nu-

- merical Recipes. The Art of Scientific Computing* (Cambridge University Press, Cambridge, 1986), Sec. 12.7.
- ³¹N. C. Barford, *Experimental Measurements: Precision, Error and Truth*, 2nd ed. (Wiley, New York, 1986).
- ³²*Handbook of Chemistry and Physics*, 76th ed. edited by D. R. Lide (Chemical Rubber, Boca Raton, FL, 1995).
- ³³M. J. Schnitzer and S. M. Block, *Nature* (London) **388**, 386 (1997).
- ³⁴C. Veigel, L. M. Coluccio, J. D. Jontes, J. C. Sparrow, R. A. Milligan, and J. E. Molloy, *Nature* (London) **398**, 530 (1999).
- ³⁵L. P. Ghislain, N. A. Switz, and W. W. Webb, *Rev. Sci. Instrum.* **65**, 2762 (1994).
- ³⁶K. Berg-Sørensen, L. Oddershede, E.-L. Florin, and H. Flyvbjerg, *J. Appl. Phys.* **93**, 3167 (2003).
- ³⁷G. G. Stokes, *Trans. Cambridge Philos. Soc.* **IX**, 8 (1851).
- ³⁸L. D. Landau and E. M. Lifshitz, *Fluid Mechanics*, 2nd ed. (Butterworth and Heinemann, Oxford, 1987), problem 5.
- ³⁹D. Bedeaux and P. Mazur, *Physica* (Amsterdam) **76**, 247 (1974).
- ⁴⁰H. Faxén, *Ark. Mat., Astron. Fys.* **17**, 1 (1923).
- ⁴¹J. Happel and H. Brenner, *Low Reynolds Number Hydrodynamics* (Nijhoff The Hague, 1983), p. 327.
- ⁴²H. A. Lorentz, *Abhandlungen über Theoretische Physik* (Druck und von B.-G. Teubner, Leipzig, 1906), Vol. 1.
- ⁴³H. Flyvbjerg (unpublished).
- ⁴⁴K. Berg-Sørensen, E. Peterman, C. Schmidt, and H. Flyvbjerg, (unpublished).
- ⁴⁵E. J. G. Peterman, M. van Dijk, L. C. Kapitein, and C. F. Schmidt, *Rev. Sci. Instrum.* **74**, 3246 (2003).
- ⁴⁶K. Visscher, S. P. Gross, and S. M. Block, *IEEE J. Sel. Top. Quantum Electron.* **2**, 1066 (1996).
- ⁴⁷F. Gittes and C. F. Schmidt, *Opt. Lett.* **23**, 7 (1998).
- ⁴⁸A. Pralle, M. Prummer, E.-L. Florin, E. H. K. Stelzer, and J. K. H. Hörber, *Microsc. Res. Tech.* **44**, 378 (1999).